Aerosol Jet Printed Strain Gauge and Temperature Compensated Strain Gauge Design

by

Chinedu Francis Dibia

A thesis
presented to the University of Waterloo
in the fulfillment of the
thesis requirement for the degree of
Master of Applied Science
in
Mechanical and Mechatronics Engineering

Waterloo, Ontario, Canada, 2018

© Chinedu Francis Dibia 2018

I hereby declare that I am the sole author of this thesis. This is a true copy of the thesis, including any required final revisions, as accepted by my examiners.

I understand that my thesis may be made electronically available to the public.

Abstract

Aerosol jet printing (AJP) is a non-contact, computer aided design (CAD) based printing that allows for an aerosol stream, being focused by a sheath gas, to print patterns on non-planar surfaces based on the specified vector path. By being able to aerosolize metal nanoparticles and sintering the nanoparticles, the patterns printed by AJP can be used as sensors. In this thesis, strain gauges were printed using AJP. The strain gauges were printed using an ink containing silver nanoparticles and after the printing process the printed samples were sintered to make the strain gauge conductive.

The underlying working principles of strain gauges and gauge factors are explored and an equation was developed to characterize the change in resistance in a strain gauge. A numerical model was also created in COMSOL to validate and complement the derived equations. The printed silver strain gauges were characterized and tested alongside standard, off-the-shelf, constantan strain gauges.

Multiple sensors were printed but only 10 fell within the data acquisition resistance range of 110 – 130 ohms. The 10 prototypes that fell within the acceptable resistance range were subjected to tensile testing. Due to variability in the machine printing process, the printed sensors were not consistent in terms of resistance and gauge factor. These challenges as well as potential solutions are discussed in this thesis. Some of the printed sensors behaved linearly and matched the performance of the standard strain gauges with only minor, explainable discrepancies. One of the printed sensors was loaded until failure and failed at a strain of 1.6%.

With the flexibility to easily change the design of the strain gauges, a new design for temperature compensation in uniaxial stress states was created and simulated using the numerical COMSOL model. This new design utilizes the poisson's ratio of the part on which the strain gauge has been mounted.

The flexibility and customization that aerosol-jet printed sensors provide presents a potential for customized strain monitoring in mechanical parts. Optimization of the printing and data acquisition processes is required to attain the reliability required to make this an ideal sensing alternative.

Acknowledgments

I would first like to thank my family for all the support they have provided me. They have always been there to listen and help in whatever way they can.

I would like to thank my supervisor, Professor Ehsan Toyserkani for granting me the opportunity to be part of this amazing project and for guiding me through the stages of the thesis.

I would also like to thank everyone on the GE Aviation project as well as everyone in the University of Waterloo MSAM lab for providing me with useful information and advice that helped me overcome some obstacles in this thesis, and for assisting me in preparing some of the samples.

In addition to that, I would especially like to thank Philippe Meszaros and Mark Griffet who are not on the GE Aviation project but were very instrumental in helping me run my experiments.

Finally, I would like to thank my friends who have been by side during this thesis.

TABLE OF CONTENTS

LIST OF FIGURES

LIST OF TABLES

CHAPTER 1

1 INTRODUCTION

Printed electronics is one of the fastest growing technologies in the world. With most industries moving towards becoming more digital, the demand for printed electronics in the production circuit boards, interconnects [1] and sensors [2] [3] keeps growing.

In sensing applications, printed electronics can be deployed to photo-based sensors [2], touch sensors [4], chemical sensors [5], mechanical sensor [6] and much more. The appeal of printed sensors lies in the flexibility of the technology. Whether the goal is to produce a high volume within a time constraint or produce low volumes with increased precision, there is a printing technology capable of achieving each goal. Some of the common printing technologies include screen printing, flexography, gravure, offset lithography, inkjet printing and electrophotography.

Inkjet printing (IJP) is one of cheaper printing techniques that require low effort to setup. However, its deposition, which is limited to droplets, makes it viable only in low-volume applications. In terms of constraints, the viscosity of the ink used in IJP must be within a certain range for the ink to be deposited from nozzle. Moreover, when depositing, IJP deposits ink in form of droplets; thus, resulting in lower line resolutions (40-166µm) [7]

Aerosol jet printing (AJP) addresses the issues of inkjet printing. By using an atomizer to aerosolize the ink, AJP can work with inks in a wider viscosity range as the screening process for the ink depends on whether the ink can be aerosolized. Furthermore, by using a sheath gas flow to drive the aerosolized ink through the nozzle and focus it to a specific spot, the resolution is significantly improved to about 10µm [8] or even less. Another advantage of

AJP and the focusing sheath gas is the ability to print on non-planar surfaces, which cannot be done using IJP.

A strain gauge is an electronic conductive sensor that is attached to a part and used to sense mechanical strain on the part. A strain gauge works on the principle of strain-induced change in resistance. A strain gauge is attached to a certain location on a part and when that location experiences deformation or strain the strain gauge deforms with the part, which then causes a change in resistance that can be monitored and used to track the strain in the part.

The focus of this thesis was to utilize AJP in printing functional strain gauges that can track the mechanical strain in the part they have been attached to or printed on. This was done by printing on a kapton substrate followed by attaching the printed strain gauge to the part. Success in this means that strain gauges can be printed directly on a part and used to sense the strain in the part. The goal of printing directly on a part makes AJP the ideal printing technique for this thesis mainly because it removes the constraint of being able to only print on planar surfaces.

1.1 Motivation

Strain gauges are mostly used to monitor localized strain on a part and for that reason, they are designed to be relatively small with an approximate surface area of $4\times2mm^2$. Strain gauges are also meant to sense strain only in one direction; although, strain gauge rosettes, which have several strain gauges on one substrate, can be purchased and used to sense strain in several directions. Strain gauges are most effective when the strain field, i.e. strain direction and strain gradient, is known. Knowing the strain field gives one an idea of what location and what orientation the strain gauge should be placed in. Without an idea of the strain field, strain gauges can miss stress concentration points or provide an average strain over a location when localized strain is required.

In order to avoid getting false readings from one strain gauge, multiple strain gauges are usually placed on parts with unknown or high strain gradients. This ensures that if one strain gauge is not properly capturing the strain field the other strain gauges can make up for it. The practice of using several strain gauges to map the strain field of a part is one that can be found in many industries such as aerospace [9] [10], civil [11], medical [12], manufacturing [13] [14] and others [15] [16].

Attaching a strain gauge to a part can be a manual and time-consuming process. Special care (as described in ref. [17]) must be taken to ensure that the strain gauge is properly bonded to the part and to ensure that there is no loss of strain transfer between the part and the strain gauge. Hence, strain field mapping using strain gauges can be a tedious task, especially when a high number of strain gauges are required [10] and each of the strain gauges have to be attached manually within a specified area.

In additional to this, conventional strain gauges are very sensitive to temperature. The temperature sensitivity is mainly due to a property known as the temperature coefficient of resistance (TCR) [18], which causes the resistivity of a material to change with temperature.

The primary focus of this thesis was to explore the use of aerosol jet printing to eliminate the excessive labor and human induced error that come with trying to mount multiple strain gauges on a specified area during strain field mapping. Moreover, in cases where the strain field is known, customized, scenario-specific strain gauge geometries can be used to effectively monitor the strain on the part. The ability to easily print customized strain gauge geometries can be utilized in printing temperature compensated strain gauge geometries that can be deployed in strain gauge applications with temperature variations. As such, the secondary focus of this thesis was to design and validate a new temperature compensated strain gauge design.

1.2 Challenges

In comparison to inkjet printing (IJP), aerosol jet printing (AJP) is a younger technology and despite the advantages that AJP has over IJP (shown in Table 1.1), IJP is still the top choice for printed electronics. The general challenges of ink deposition technologies have been described in ref. [19], but listed below are the challenges specific to this thesis:

Table 1.1: Comparison of the Main Characteristics of AJP and IJP (↑ Indicates High, ↓ Indicates Low) [20]

characteristic	IJP	AJP
ink flexibility concerning particle material, particle loading, particle size, ink viscosity, and ink surface tension	↓	↑
ink consumption, including dead volume of the deposition system and "overspray"	↓	↑
suitability for thin layer deposition (considering a certain ink formulation as demonstrated in this contribution)	↓	↑
suitability for thick layer deposition (considering a certain ink formulation as demonstrated in this contribution and only one pass)	↑	↓
achievable layer thickness and layer width range (considering one nozzle and one pass)	↑	↓
edge sharpness of deposited layers	↑	↓
deposition velocity (in principle, based on the deposition mechanism comparing drop-on-demand IJP and AJP)	↓	↑
scalability of the deposition system, especially toward large area processing	↑	↓
flexibility concerning substrate materials and substrate topology (e.g., 3D substrates)	↓	↑
system costs considering single-nozzle deposition systems with similar features (e.g., concerning axis accuracy, etc.)	↓	↑

1. Ink formulation: For IJP, the focus is on creating an ink that falls into the right viscosity range. For AJP the ink should be capable of being aerosolized; therefore, for metallic inks that are made with metal nanoparticles, the ink needs to contain stabilizers that prevent the metal nanoparticles from agglomerating and the stabilizers being used also should capable of being aerosolized.

2. Machine and process reliability: In AJP, the aerosolizing process is very important because without this process there can be no deposition from the nozzle. However, very minor changes in the ink formulation can cause significant changes in the amount of material being aerosolized. This will cause a change in the material deposition from the nozzle, which can lead to significant variance from one sensor to the next.

3. Effects of heat treatment and sintering: After printing with a metallic ink, the printed sensor is subjected to a heat treatment that is meant evaporate the solvent and stabilizers while forming sinter necks [21] between the metal nanoparticles. Since material deposition is not monitored it is possible for there to be variations in the ratio of deposited solvent to deposited metal nanoparticles. This variation entails that, during the sintering process of a sensor printed with less metal nanoparticles, there are likely going to be more pores due to the evaporated solvents and stabilizers. There will also be less sinter necks due to the presence of less metal nanoparticles. This can potentially result in sensors with higher electrical resistance, higher strain sensitivity and lower elongation before failure. The variance in printed sensors presents a challenge in characterizing the sensors.

1.3 Objectives and Goals

The main objectives of this thesis are as follows:

1. Develop and validate a numerical model for predicting the performance of a strain gauge with conventional and unconventional geometries

2. Use an aerosol jet printer to successfully print strain gauges on a kapton substrate and compare the performance of the printed strain gauges to the performance of conventional strain gauges

3. Use an aerosol jet printer to successfully print strain gauges directly on a test part and compare the performance of the printed strain gauges to the performance of conventional strain gauges

4. Characterize the printed strain gauges

The secondary objective is to:

5. Develop a new temperature compensated strain gauge geometry and validate the performance of this new geometry

In order to term the above listed objectives as 'successful' the following preliminary goals should be achieved:

a. Since the equipment available for strain gauge data acquisition only works with strain gauges in a specific resistance range, printed sensor should have a resistance that falls in the range of conventional strain gauges i.e. 110 – 130ohms

b. Printed sensors need to have a linear response to strain like conventional strain gauges

c. Printed sensors should have a strain sensitivity (gauge factor) close to or higher than that of conventional strain gauges. The sensitivity should be no less than 50% of conventional strain gauges. Anything lower than 50% would require special instrumentation to sense the significantly small changes in resistance

d. Temperature compensated strain gauge design should produce resultant strain values that represent the mechanical strain on the part regardless of environment temperature

1.4 Contributions

This thesis explores the performance of aerosol jet printed strain gauges. The strain gauges are printed using an ink containing silver nanoparticles. The advantage of printing sensors using a CAD based printing technique lies in the flexibility and ability to design and print

customized strain gauge geometries. Unlike other printing techniques, customized geometries that are specifically made to capture the strain field of different scenarios can be produced by simply modifying a CAD file. The ability to print sensors also eliminates the tedious labor that goes into mounting multiple strain gauges for applications like strain field mapping.

1.5 Summary of Thesis Plan

The work done for this thesis can be divided into stages as follows:

1. A numerical model is developed in COMSOL and compared to the analytical model in Section 3.1. A correction factor is introduced to calibrate the model and account for any unknown properties. The purpose of this model is to simulate the performance of new strain gauge geometry designs without having to print and test each design; thereby, providing a simplified screening process.

2. Strain gauges with the standard strain gauge geometry are printed using the Optomec aerosol jet printer. The first strain gauges are printed on a kapton substrate using a silver ink from Novacentrix and are sintered on a hot plate.

3. The strain gauges are then attached to steel tensile test coupons, which are then subjected to tensile loading. The data from strain gauges are collected using the DAQ setup described in Section 2.3.4 and the performance of the printed strain gauges are compared to the performance of conventional strain gauges purchased from Micro-measurements.

4. A temperature compensated strain gauge design for a uniaxial stress state is developed and validated using the same model developed in stage 1.

1.6 Thesis Layout

This thesis is separated into 5 chapters. This chapter covers the general idea of the field being investigated, the motivation, the challenges, the objectives of the thesis and the intended goals. Chapter 2 provides background information on aerosol jet printing, the Optomec M^3D, which is the printer being used for this thesis, and the general process of printing a working sensor. Chapter 2 also covers strain gauges, its working principle, typical strain gauge geometries, typical temperature compensation techniques and data acquisition from a strain gauge. Chapter 3 describes an FEA model that was created in COMSOL and used to simulate the performance of a strain gauge. The aim of this model was to have a model that accurately predicted strain gauge performance so that future geometry designs could be simulated with the model before printing.

Chapter 4 contains the test equipment, procedures and additional challenges that came with testing the printed sensors. It also contains the results and discussion for the characterization and testing of the printed sensors. Chapters 5 focuses on the temperature compensated design and describes the COMSOL model that was used to prove the validity of the design. Chapter 6 presents the conclusions that can be drawn from this thesis as well as the future works that can be done to improve the performance of printed strain gauges.

CHAPTER 2

2 BACKGROUND

2.1 Printed Electronics

Printed electronics refers to an electrically functional ink deposited on a substrate to facilitate connection between electrical components (passive) or to serve as a sensing device (active). Printed electronics offer a cheap, high-production solution to the deployment of electronic circuits and sensors. They also offer significant design flexibility that allows them to be easily customized for the required application. Advancements in technology allow printed electronics to be incorporated into several fields and applications. Some common applications of printed electronics include; the production of flexible displays, wearable electronics [22], low-cost RFID systems and thin film transistors, capacitors [23] and resistors, which can be used on circuit boards.

Common methods of producing printed electronics include screen printing, flexography, gravure, offset lithography, inkjet printing and electrophotography. Descriptions and schematics of each process can be found in ref. [7]. In inkjet printing (IJP), the ink is deposited from a nozzle unto a substrate, meaning that only a spot size of material is being deposited at any given time. As such, the throughput from this process is lower than other common printing techniques. The primary constraints of IJP are; it only works with inks in a certain viscosity range ($< 10^{-2}$ Pa.s [7]) and the resolution is relatively low with a minimum line width of approximately 166μm for continuous printing [7]. Although, for certain setups and materials, IJP can achieve a line width as low as 15μm [24].

2.2 Aerosol Jet Printing

AJP is a CAD based, non-contact printing that deposits material onto a substrate based on a vector path specified within the CAD file. AJP works by aerosolizing an ink (i.e. turning the ink into vapor using an atomizer) and then using two gas flows to deposit the ink onto a substrate. The first gas flow, which is known as the atomizer gas flow, is used to carry the aerosol from the aerosolizing chamber to the nozzle where the second gas flow, known as the sheath gas flow, focuses the aerosol to a spot. A schematic of the process being used for graphene ink can be seen in Figure 2.1.
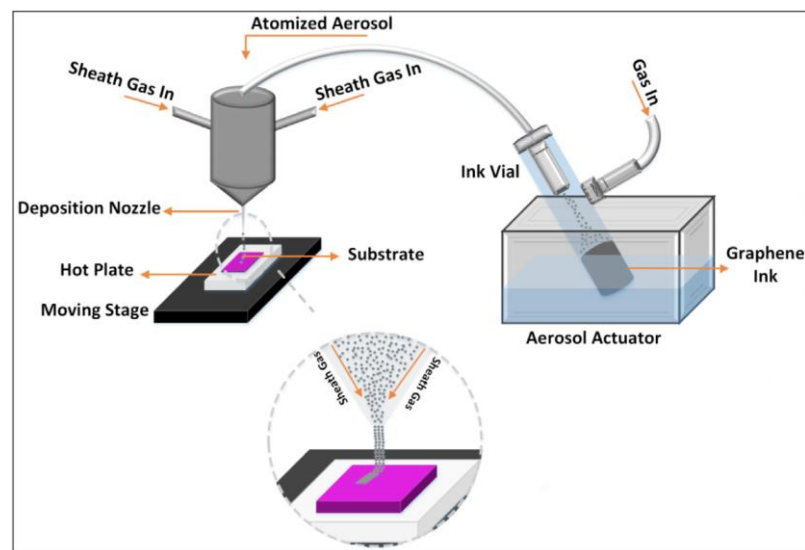
Figure 2.1: Aerosol-jet printing setup [25]

With the primary working principle of AJP being the aerosolization and focusing of the aerosolized ink, the primary constraints of inkjet printing are eliminated because the viscosity of the ink becomes less of a critical factor and the focusing sheath gas allows for higher resolution. Although the maximum achievable layer thickness for AJP falls in the 1μm range [20], AJP excels in line width resolution, which can be as low as 10μm [8]. Another major advantage of AJP is the ability to print on non-planar surfaces. With the sheath gas focusing the aerosol, the resolution can be maintained for a nozzle to substrate

distance of 5mm or more [26]. The actual allowable distance is dependent on the nozzle type, ink and other parameters [26].

Although AJP is a younger technology compared to inkjet printing, AJP has been successfully used in projects for printing sensors [2] [3] [4], graphene interconnects [25], carbon nanotube transistors [27], and memristors from nanowire composites [28], amongst several other projects.

2.2.1 Optomec System

For this thesis, the Optomec M^{3}D aerosol jet printer was used and a labelled diagram is shown in Figure 2.2. The Optomec M^{3}D consists of two translational tables; one table carrying the substrate and translating only in the y-direction and another table carrying the nozzle head and translating only in the x-direction. These translational tables are driven nano-precision piezoelectric motors and as such, have a precision of 1nm. The distance from the nozzle to the substrate can be adjusted manually before the printing process begins.
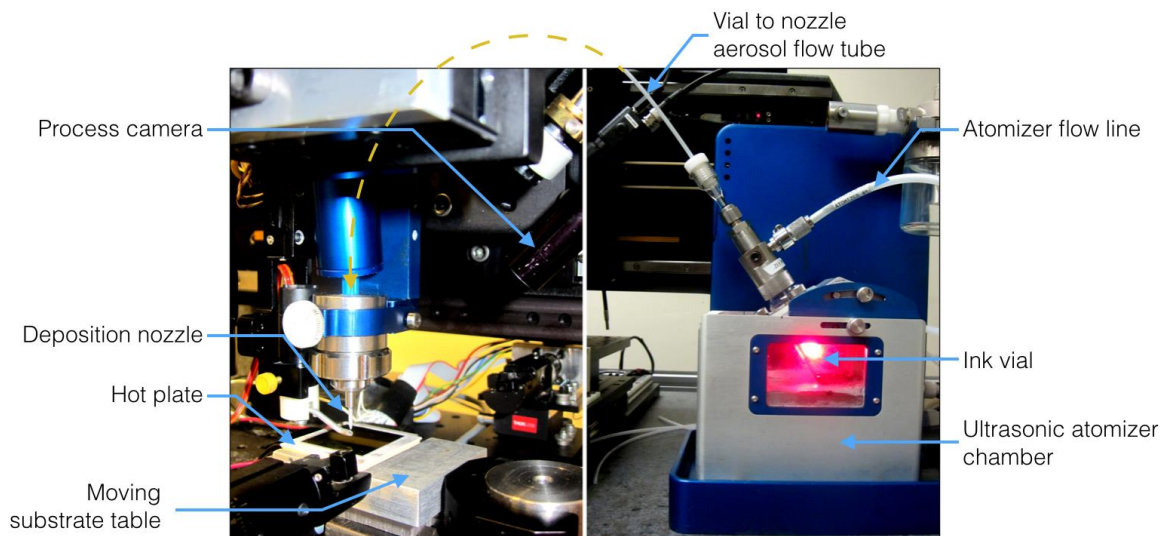
Figure 2.2: Optomec M^{3}D Schematic

A hot plate has been added to the y-axis translation table to heat the substrate and evaporate some of the solvent during printing. This reduces excessive wetting and flow of the printed material and ensures that the desired resolution is attained.

The Optomec M^{3}D holds the ink in a vial that is placed in an ultrasonic atomizer chamber. The ultrasonic atomizer chamber uses the water in the chamber to atomize or aerosolize the ink in the vial. The atomized ink forms vapor that is then carried as an aerosol to the nozzle by a nitrogen atomizer gas. At the nozzle, a nitrogen sheath gas flow is introduced and used to focus the aerosol to a specific spot on the substrate.

A more detailed description of the system and process as well as successful demonstrations can be found ref. [26]. Some of the demonstrations using this system can be seen in Figure 2.3.

Figure 2.3: Demonstrations of Optomec M^{3}D Aerosol Jet Printer: (Left) Digital thermometer on PA10 thermoplastic, (Right) Detail of capacitive sensor structure

2.3 Strain Gauges

The simplified definition of a strain gauge is an electrically conductive strip or wire that changes resistance when deformed. The strain gauge is carefully secured to a part that undergoes deformation so that when the part undergoes the deformation, the strain gauge

undergoes the same amount of deformation, which then results in a change in resistance that can be used to predict the strain on the part.

Conventional or standard strain gauges are most commonly made from etching a very thin sheet (~7μm) of constantan (Cu-Ni alloy), which has been attached to a polyimide or kapton substrate. Another layer of polyimide is usually placed over the etched strain gauge (as shown in Figure 2.4) to encapsulate and protect it.
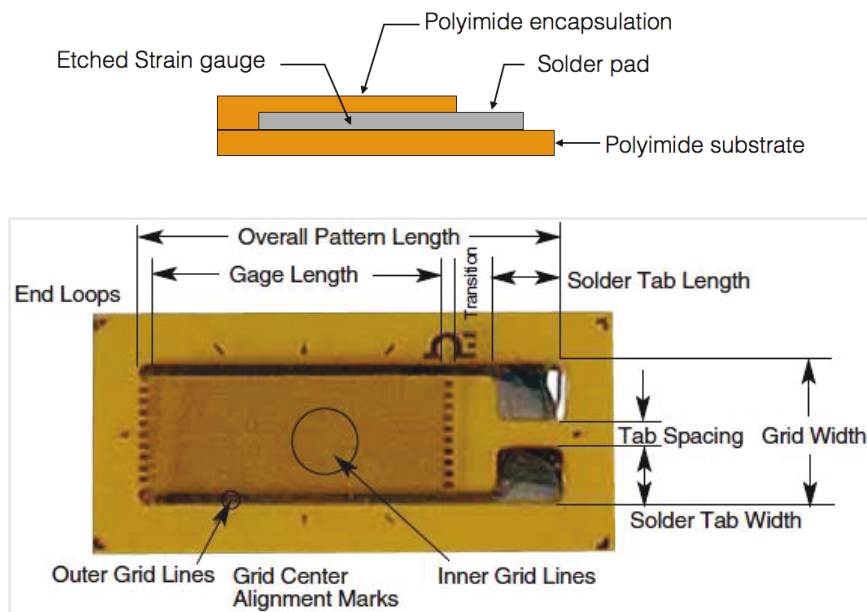
Figure 2.4: (Top) Conventional Strain Gauge Assembly and (bottom) Labelled Strain Gauge Diagram [29]

2.3.1 Working Principle and Gauge Factor

Basic strain gauges are made to sense strain in one primary axis, which is the axis parallel to the strain gauge grids. Majority of the change in resistance comes from the deformation of the strain gauge inner grids (Figure 2.4) along its primary axis. A change in length of the grids will result in the most change in resistance. Theoretically speaking, a change in cross-sectional area should result in a higher change in resistance but, in reality, the strain on the

part that occurs perpendicular to the primary axis does not properly get transferred to the strain gauge grids as will be shown and discussed in Section 3.4.1.

The gauge factor, *GF,* is a property that is used to describe the sensitivity of a strain gauge and relate the strain on the part, ε, to the change in resistance in the strain gauge, ΔR.

$$GF = \frac{\Delta R}{R_0 \varepsilon} \quad where, R_0 \ is \ the \ original, undeformed \ resistance \ of \ the \ strain \ gauge$$

2.3.2 Strain Gauge Geometries

While basic strain gauges are meant to sense strain in one axis, strain gauge rosettes are made up of several strain gauges with the grids oriented in a certain way to effectively capture specific strain fields. Different strain gauge geometries are shown in Figure 2.5 and a brief functional description is given for each geometry.

(a)

(b)

(c)   (d)   (e)
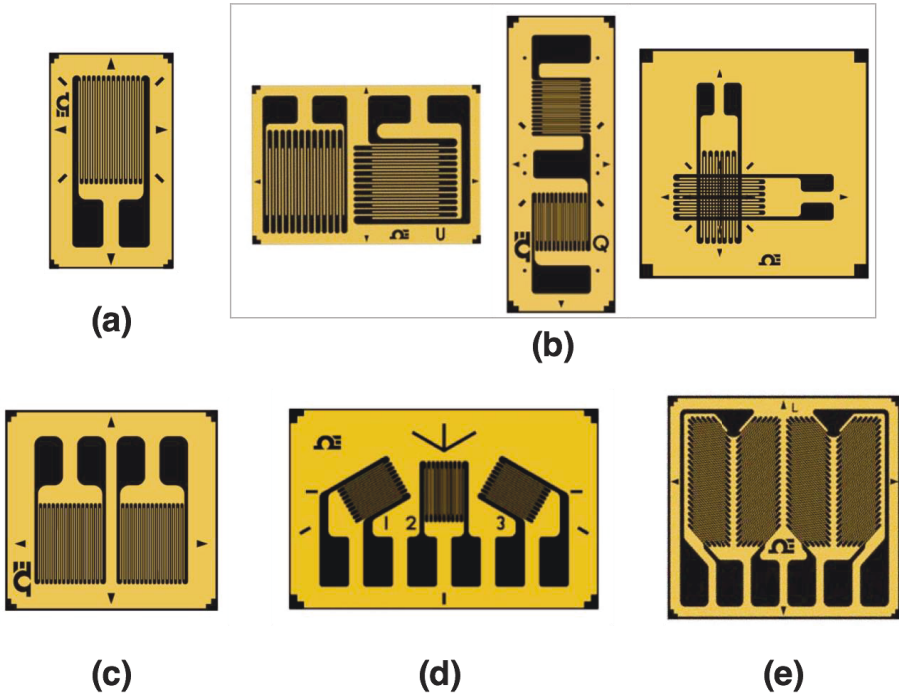
Figure 2.5: Different Strain Gauge Geometry Designs [30]

    a)   1-Axis General Purpose Strain Gauge; used for measuring strain in one axis.

b) Dual 90º (Tee Rosette) Strain Gauge; used for measuring strain in two known principal axes. Tee rosettes comprise of two separate unconnected or connected strain gauges that are perpendicular to each other. The two strain gauges can also be overlapping when there are space constraints.

c) Dual Parallel Strain Gauge; used for signal amplification of strain measurements in one axis.

d) Strain Gauge Rosette; used to determine the value and direction of principal strains when the principal axes are unknown.

e) Torque and Shear Gauges; oriented at 45º to the principal axis and used to measure shear strains

2.3.3 Temperature Compensation Techniques

The temperature coefficient of resistivity (TCR) [18] [31] causes a material to change its resistivity with temperature. This change in resistivity leads to a change in resistance that indicates a higher strain value than what is actually being experienced by the part. The effect of the TCR can sometimes result in a strain reading that is ten times higher than the actual mechanical strain on the part. Strain gauge temperature compensation techniques are used to reduce or accommodate the temperature sensitivity of strain gauges. There are two common temperature compensation techniques:

1. **Self-Temperature Compensated (S-T-C):** This technique works on the principle of trying to make the TCR, close to zero for a certain temperature range (usually the operating temperature range). A TCR vs. temperature curve (Figure 2.6) resembles a backward S for most metals. However, with selective heat treatment of the gauge alloy, the curve can be rotated (usually about 75ºF) and made flat for a certain temperature range as shown in Figure 2.6.

2. **Dummy Gauge Temperature Compensation:** The idea behind this technique is to use two strain gauges in which, one of the strain gauges is sensitive to mechanical strain but the other is insensitive or less sensitive to mechanical strain. However, both

strain gauges have the same response to changes in temperature and the total response of the mechanically insensitive strain gauge can be subtracted from that of the mechanically sensitive gauge to result in a response that only represents the mechanical strain. The most basic example of this is using a dual 90° (tee rosette) strain gauge to sense strain in a uniaxial strain field. The primary strain gauge, which is aligned with the strain field, will experience mechanical strain whereas the secondary strain gauge experiences nothing. However, both strain gauges will experience the effects of temperature and the secondary strain gauge can be used to adjust the response of the primary strain gauge to show only the mechanical strain-induced response.
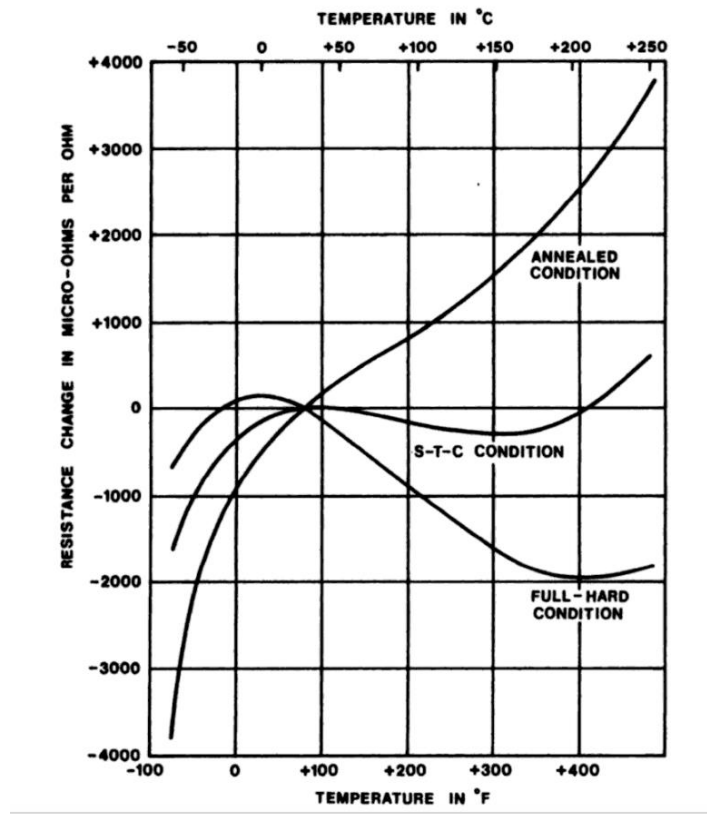
Figure 2.6: Representative Change in Thermal-Induced Resistance Output Characteristic of Constantan Alloy Due to Heat-Treatment [32]

16

2.3.4 Data Acquisition

Collecting data from a strain gauge is done through an electrical circuit. A voltage is applied to the strain gauge on one end and a readout voltage is collected at the other end. The two most common data acquisition electrical circuits are the half bridge and full bridge circuits shown in Figure 2.7. **V** is the excitation voltage applied to the system whereas $\mathbf{E_o}$ is the readout voltage. $\mathbf{R_g}$ represents the active strain gage which will be mounted on the part being observed. The change in strain gage resistance creates a $\mathbf{\Delta E_o}$ that serves as an indicator for the induced strain. $\mathbf{R_B}$ (half-bridge circuit) and $\mathbf{R_2}$ to $\mathbf{R_4}$ (full-bridge circuit) can also be strain gages used for temperature compensation, amplifying the output or both
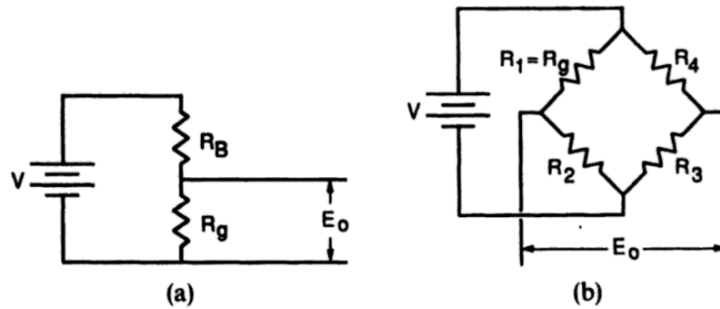
Figure 2.7: (a) Half-bridge (Potentiometric) Circuit and (b) Full-bridge (Wheatstone) Circuit [32]

- **Half-Bridge Circuit:** These are more commonly used to measure dynamic strain because the change in readout voltage, ΔE_o, is usually significantly smaller than E_o and there are no readily available readout devices capable of measuring ΔE_o to a desirable accuracy. However, when measuring dynamic strains, a high pass filter can be used in the output to block out E_o and only record the changes to ΔE_o. This method does however eliminate any permanent ΔE_o that the system may acquire.

$$\Delta E_O = V \frac{a}{(1+a)^2} \left[\frac{\Delta R_g}{R_g} - \frac{\Delta R_B}{R_B} \right] (1-n)$$

Where,
n = nonlinearity term,   a = R_B/R_G
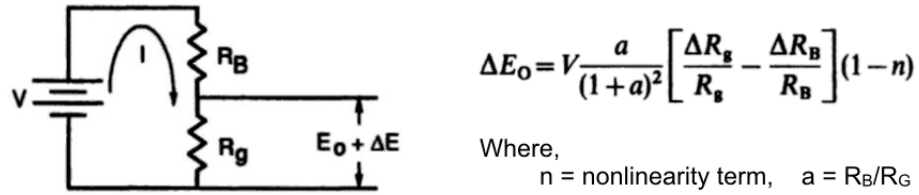
Figure 2.8: Half-bridge Circuit and Half-bridge Equation [32]

For temperature compensation, R_B (as shown in Figure 2.8) is replaced with another strain gage, equal in resistance to R_g but mounted perpendicular to R_g. Hence, when mechanical strain is induced, ΔR_g increases or decreases and ΔR_B is approximately 0. However, when thermal strain is introduced it will affect both gages the same way and the ΔR from thermal strain cancels out as per the equation in   Figure 2.8.

- **Full-Bridge Circuit:** With a full-bridge circuit, the initial readout voltage, E_o, can be made zero by making $R_1 = R_2$ and $R_3 = R_4$. By doing so, static and dynamic strains can be measured since the readout device only needs to accurately measure ΔE_o without worrying about an initially higher E_o.

$$\Delta E_O = V \frac{a}{(1+a)^2} \left[\frac{\Delta R_1}{R_1} - \frac{\Delta R_2}{R_2} + \frac{\Delta R_3}{R_3} - \frac{\Delta R_4}{R_4} \right] (1-n)$$

Where,
n = nonlinearity term,   a = $R_1/R_2 = R_4/R_3$
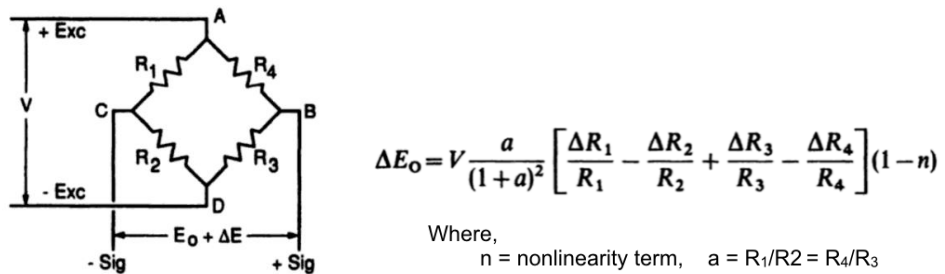
Figure 2.9: Full-bridge Circuit and Full-bridge Equation

For temperature compensation, R_1 and R_2 (as shown in Figure 2.9) can be mounted perpendicular to one another so that the ΔR induced by thermal strain is equivalent between R_1 and R_2, and cancels out; thereby, producing a total ΔR free of thermal effects.

18

For amplification of the output, R_1 and R_3 can be mounted in the same orientation to duplicate the change in resistance. R_2 and R_4 can then be mounted perpendicular to R_1 and R_3 to provide thermal compensation to both R_1 and R_3. In the case of bending strains, R_1 and R_2 are mounted in the same orientation but on opposite sides of the plate. This way R_1 sees tension while R_2 sees compression and the change in resistance adds up to create an amplification in the total ΔR recorded.

The embodiment of these electrical circuits are in data acquisition systems also referred to as DAQs. For this thesis, the NI-9237 DAQ from National Instruments was used. Since most of the experiments done for this thesis were done on single strain gauges, a bridge completion circuit that provides R_2 to R_4 (as per Figure 2.9) was required. The NI-9944, a bridge completion accessory for strain gauges in the 120ohm range was used. A schematic of the setup and connections can be seen in Figure 2.11.
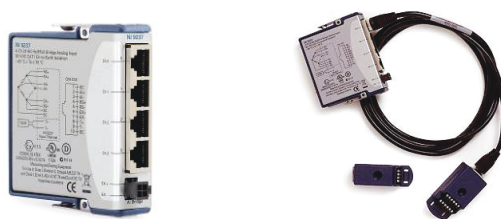
Figure 2.10: (Left) NI-9237 DAQ and (Right) NI-9237 DAQ Connected to NI-9944 Bridge Completion Accessory [33]
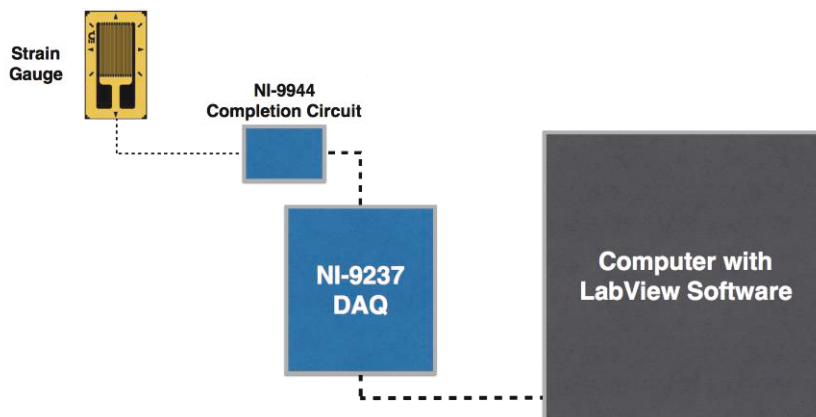
Figure 2.11: Complete Data Acquisition Schematic

2.4 Chapter 2 Summary

In this chapter, a brief discussion on printed electronics and printing technologies was discussed. This was followed by an exploration of the aerosol jet printing process and the Optomec M^{3}D aerosol jet printer.

The working principle of a strain gauge was discussed and the functions of various strain gauge geometries were highlighted. Some temperature compensation techniques were covered and the process of acquiring data from a strain gauge was described.

CHAPTER 3

3 MODELLING OF STRAIN GAUGE PERFORMANCE

3.1 Strain Gauge Grid Performance Analytical Model

In order to have a complete understanding of strain gauge performance, an analytical model based on the partial differential of the resistance of a wire was investigated. The goal of this model was to have a basis that could be used to identify all the required properties for the numerical model and could also be used to validate the results of the numerical model. The analytical model takes a single strain gauge grid as a rectangular prism wire subjected to uniaxial strain and derives an equation for the resulting change in resistance. The analytical model is as follows:
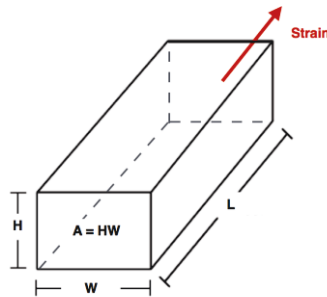
Figure 3.1: Single Grid Approximation with Strain in the Axial Direction

$$R = \rho \frac{l}{A},\tag{3.1}$$

Strain from part underneath strain gauge grid $= \varepsilon_l \; or \; \varepsilon_{axial}$

21

$\rightarrow \Delta R = \frac{\partial R}{\partial l} dl + \frac{\partial R}{\partial A} dA + \frac{\partial R}{\partial \rho} d\rho = \frac{\rho}{A} dl - \frac{\rho}{A^2} dA + \frac{l}{A} d\rho$

$\rightarrow \frac{\Delta R}{R} = \frac{dl}{l} - \frac{dA}{A} + \frac{d\rho}{\rho}$

Where $R = R_0 = \rho \frac{l}{A}$

$\rightarrow$ *Aside*: $\frac{dl}{l} = \varepsilon_l$

$\rightarrow$ *Aside*: $\frac{dA}{A} = \frac{(H+dH)(W+dW)-HW}{HW} = \frac{H(-v\varepsilon_l W)+W(-v\varepsilon_l H)+[(-v\varepsilon_l)^2 HW\approx 0]}{HW} \approx -2v\varepsilon_l$

Where $v =$ poisson's ratio of the strain gauge grid

$\rightarrow$ *Therefore*: $\frac{\Delta R}{R} = \frac{dl}{l} - \frac{dA}{A} + \frac{d\rho}{\rho} \approx \varepsilon_l + 2v\varepsilon_l + \left(\frac{d\rho}{\rho}\right)_{axial}$

$\rightarrow \Delta R \approx \varepsilon_l(1 + 2v)R + \left(\frac{d\rho}{\rho}\right)_{axial} R$ (3.2)

$\rightarrow \Delta R \equiv Geomtric\ Factor + Piezoresistive\ Factor$

It can be seen from the derivation that for small strains the resultant change in resistance is a combination of the geometric deformation of the strain gauge grid as well as a strain-induced change in resistivity (piezoresistive). Additional derivations for strain perpendicular to the grid and for biaxial strain can be found in Appendix A.

3.2 COMSOL Numerical Model

The aim of this numerical model was to simulate the performance of a strain gauge and compare the results from the model to both the analytical results from Section 3.1 and

practical results from physically testing a conventional strain gauge. The model was made up of a conventional strain gauge assembly (as described in Section 2.3) attached to a steel tensile test coupon and subjected to tensile loading. Two main models were created; one with the strain gauge's primary axis aligned with the direction of the primary strain (axially oriented strain gauge) and one with the strain gauge's primary axis perpendicular to the direction of the primary strain (transversely oriented strain gauge). Upon noticing deviations between the transversely oriented strain gauge model and the analytical results, two additional models with uniaxial strain states were created. The data collected from these models were the strain on the part and the change in resistance of the strain gauge. With this data, the gauge factor was calculated.

These models focused on the geometrically-induced change in resistance that a strain gauge experiences when subjected strain. The piezoresistive change in resistance, which involves a material's change in resistivity due to deformation of the lattice structure [34], was not incorporated in the model due to the complexity of incorporating that feature into the model. The piezoresistive change in resistance was also not considered in the model because there were no discovered papers or documents that provided the piezoresistive property value of constantan or silver. However, a correction factor that was determined from experiment was introduced to account for the piezoresistive effect.

3.2.1 Design and Material

The model comprises of a conventional constantan strain gauge encapsulated in polyimide and mounted to a steel 1018 tensile test coupon as shown in Figure 3.2. The dimensions of the strain gauge can be found in Appendix B.

The material assembly and thickness values shown in Figure 3.2 are derived from ref. [35]. The material properties of each material used is shown in Table 3.1 along with source of each material property. The dimensions of the tensile coupon are the dimensions of the readily available tensile coupons available in the University of Waterloo, Engineering 3, Materials Lab. The dimensions can also be found in Appendix B.

Since the strain gauge is encapsulated by the polyimide and the assembly is mounted to the tensile coupon using a strong glue, the assembly is united together using the 'Form-Union' function in COMSOL. This means that adjacent parts in contact share a single boundary and as such, deformation in the boundary of one part should be completely transferred to the next part as long as both parts share the same boundary.
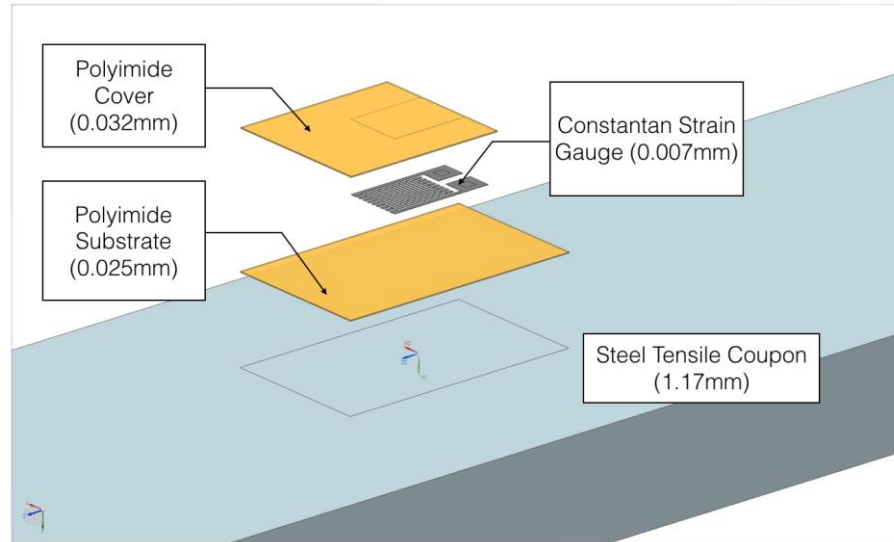
Figure 3.2: Strain Gauge Assembly

Table 3.1: Material Properties

Property	Material		
	Steel 1018 [36]	Polyimide [37]	Constantan [38]
Young's Modulus	205GPa	2.5GPa	162GPa
Poison's ratio	0.285	0.34	0.327
Resistivity	N/A	N/A	490e-6ohm.cm

3.2.2 Boundary Conditions

For the loading conditions, one end of the tensile test coupon is fixed while the other end is subjected to a tensile force as shown in Figure 3.3. The applied tensile force is varied to result in different strain values underneath the strain gauge with the maximum strain being

3%. The maximum strain value of 3% strain represents the maximum operating strain of the conventional strain gauge model used in this simulation [35].

Two models are run; one with the strain gauge mounted axially (parallel to the loading direction and strain field) and one with the strain gauge mounted transversely (perpendicular to the loading direction and strain field). The predicted deformation of the axially mounted model is an elongation in strain gauge grid and shrinkage of the cross-sectional area. However, the transversely mounted model was created to determine whether loading a strain gauge along an axis perpendicular to its primary axis had a significant effect on the change in resistance. This would help determine what to consider in future strain gauge designs.
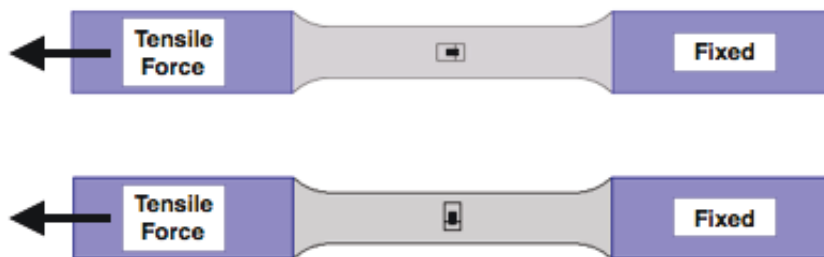
Figure 3.3: Loading and Boundary Conditions for Axially (Top) and Transversely (Bottom) Mounted Strain Gauges

3.2.3 Meshing

The geometry was meshed using a sweep mesh with triangular elements. The sweep mesh was done along the thickness of the part; thus, resulting in triangular prism elements. The strain gauge assembly was meshed with an 'extremely fine' sized mesh while the test coupon was meshed with a 'fine' sized mesh. The sweep mesh was made to have a distribution of 1 along the strain gauge and substrate thicknesses, and a distribution of 4 along the tensile coupon thickness as shown in Figure 3.4. A mesh dependency study was also done to ensure that there was no numerical error being introduced by the meshing process. The mesh independency study models were meshed with an 'extra fine' triangular sweep mesh and an

'extremely fine' free tetrahedral mesh as shown in Figure 3.4. All meshes produced the same result.
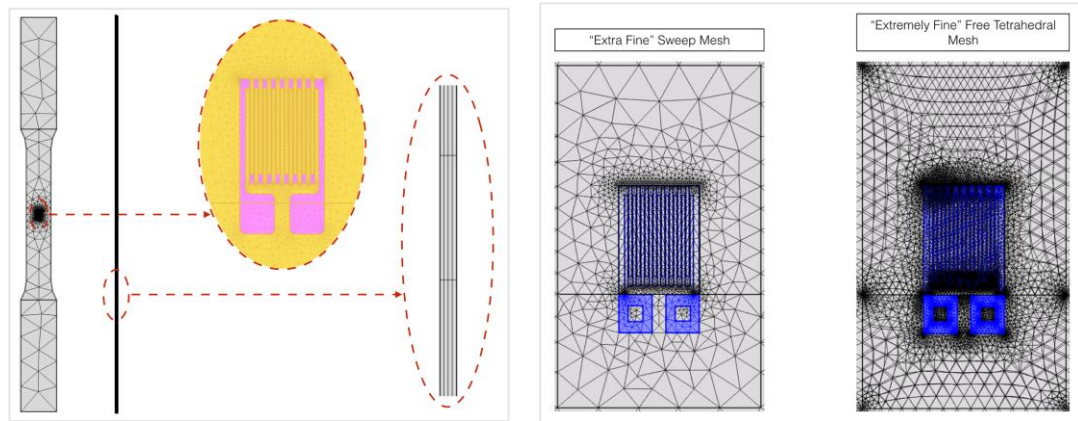
Figure 3.4: (Left) swept triangular mesh of strain gauge assembly and test sample. (right) mesh independency study

It was important to put a fixed number of mesh elements on the strain gauge grids, so that every time the model was remeshed for change in resistance extraction the grids had the same number of elements and produced an accurate result that was relatable to the previous resistance readings. For this thesis, the grids were given 45 mesh elements.

3.2.4 Resistance Extraction
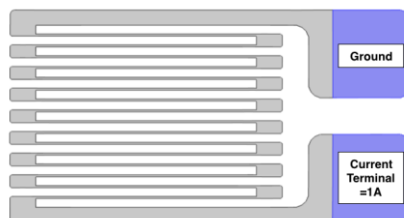
Figure 3.5: Current being applied to deformed strain gauge to get initial or new resistance value

The change in resistance of the strain gauge was extracted by taking the deformed geometry from the mechanical simulation, remeshing that deformed geometry and exporting that mesh into an electrical simulation. The obtained change in resistance is solely geometric because

it is attained based on the deformation of the strain gauge and nothing more. With the deformed geometry, only the strain gauge is left behind while all the other parts are deleted. As per Figure 3.5, a current of 1A is applied to the strain gauge to get the electric potential, V, which relates to the resistance (i.e. V=IR or R=V/I).

3.2.5 Review of Equations

As described in the derivation in Section 3.1, the change in resistance of a strain gauge grid comprises of two parts:

i.   The geometrical part that is caused by the grid's change in shape (elongation, cross-sectional shrinkage etc.).

Recall from equation *3.2*, $\Delta R_{geometric} = \varepsilon_l(1 + 2v)R$

$$\therefore GF_{geometric} = (1 + 2v) \tag{3.3}$$

ii. The piezoresistive part, which is a result of the strain gauge material changing its resistivity, ρ, due to the deformation of the lattice structure.

Recall, $\Delta R_{piezoresitive} = \left(\frac{d\rho}{\rho}\right)R$

$$\therefore GF_{piezoresitive} = \frac{d\rho}{\rho\varepsilon} \tag{3.4}$$

While piezoresistivity is neither common nor dominant in metal or metal alloys, the derived analytical equation shows that it is a factor to be considered. It will be shown later in this thesis that there is a piezoresistive effect that accounts for ~25% of the total change in resistance.

Since the piezoresistive property, $d\rho/\rho\varepsilon$, was unknown, a correction factor, C_{pz}, was introduced to make the geometric change in resistance represent the total change in resistance;

$$\therefore \Delta R_{total} = C_{pz}\Delta R_{geometric} = C_{pz}\varepsilon_l(1 + 2v)R \tag{3.5}$$

3.2.6 Results
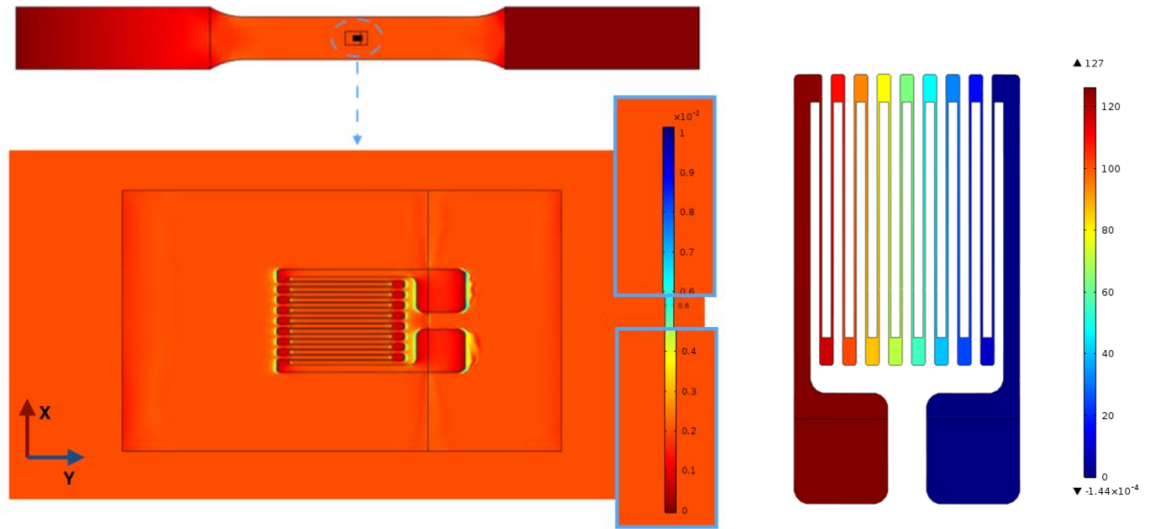
Figure 3.6: COMSOL result for axially mounted model showing strain field (left) and electric potential for resistance study (right)

Table 3.2: Axially mounted model results (in tension) and comparison to analytical results

Strain				Resistance	Gauge Factor	
Target Axial	Y-dir	X-dir	Z-dir	R0 = 120.66	GF COMSOL	GF (*eq 3.3*)
0.002	0.0020	-0.0006	-0.0007	121.06	1.663	
0.016	0.0157	-0.0045	0.0052	123.805	1.660	**1.654**
0.030	0.0291	-0.0083	-0.0095	126.5	1.661	

Table 3.3: Axially mounted model results (in compression) and comparison to analytical results

Strain				Resistance	Gauge Factor	
Target Axial	Y-dir	X-dir	Z-dir	R0 = 120.66	GF COMSOL	GF (*eq 3.3*)
-0.002	-0.0020	0.0006	0.0007	121.06	1.650	
-0.016	-0.0163	0.0046	0.0053	123.805	1.675	**1.654**
-0.030	-0.0309	0.0090	0.0010	126.5	1.693	

As shown in Figure 3.6, the strain on the strain gauge matches the target strain of 0.2% and the resistance is around 120ohms. The tensile force was varied to induce different strain values and attain different resistance values. These results were then used to calculate the gauge factors shown in Table 3.2 and these attained gauge factors were compared to the analytical model that produced *equation 2* in Section 3.2.5. The strain gauge's poisson's ratio is set to 0.327 as stated in Table 3.1.
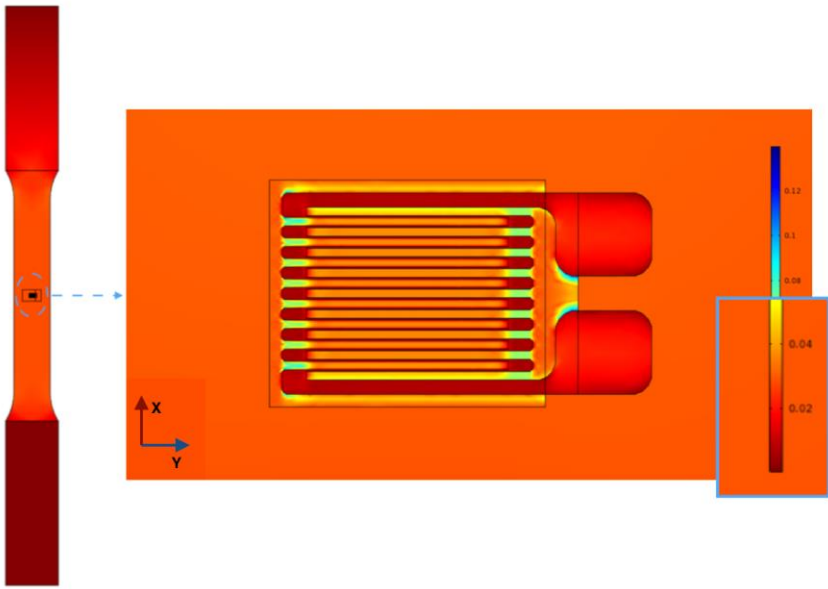
Figure 3.7: COMSOL result for transversely mounted model showing strain field

Table 3.4: Transversely mounted model results (in tension) and comparison to analytical results

Strain				Resistance	Gauge Factor	
Target Transverse	Y-dir	X-dir	Z-dir	R0 = 120.70	GF$_t$ COMSOL	GF$_t$ (*eq 3.3*)
0.002	-0.0006	0.0020	-0.0007	120.589	-0.467	
0.016	-0.0045	0.0157	0.0052	119.803	-0.465	**-1**
0.030	-0.0083	0.0291	-0.0095	119.047	-0.457	

29

Table 3.5: Transversely mounted model results (in compression) and comparison to analytical results

Strain				Resistance	Gauge Factor	
Target Transverse	Y-dir	X-dir	Z-dir	R0 = 120.70	GF_t COMSOL	GF_t (*eq 3.3*)
-0.002	0.0006	-0.0020	0.0007	120.818	-0.482	
-0.016	0.0046	-0.0163	0.0053	121.636	-0.483	**-1**
-0.030	0.0009	0.0309	0.0010	122.471	-0.488	

For the transversely mounted model, it can be seen from Figure 3.7 that the strain in the strain gauge is lower than the strain in the surrounding parts. The transverse gauge factor, GF_t was calculated as:

$GF_t = \Delta R/R\varepsilon$; where ε is the primary strain acting perpendicular to the strain gauge grids

For this model, GF_t was lower than expected, with an average of **-0.473** rather than **-1** (as per Appendix A). This led to questions regarding whether the transverse strains from the tensile coupon had any real effect on the strain gauge performance.

3.3 Uniaxial Strain Cube Model Verification

The analytical model in Appendix A suggests that the gauge factor for a strain gauge grid subjected to only transverse loading should be approximately -1. However, the COMSOL results for the transversely oriented strain gauge on the tensile coupon, which is a biaxial strain state with the primary strain acting transversely on the strain gauge, shows that the gauge factor is far from the expected value. To truly understand the effect of transverse strain, a cube model with a uniaxial strain state was created. The aim of this model was to see if there was any significant change in resistance in a strain gauge subjected to only transverse strain.

3.3.1 Design, Meshing and Loading Conditions

The model was a 10mm cube with a conventional strain gauge assembly mounted on top. The cube was given properties of steel 1018 and the properties of the strain gauge assembly were the same as the previous models. The meshing was done using a triangular mesh that was swept from top to bottom to result in triangular prism elements. With the primary strain in the strain gauge grids expected to be smaller than the primary strain in previous models, the strain gauge grids were given 55 mesh elements for improved accuracy. For the loading, the right cube wall was fixed while the left wall was displaced to cause a certain amount of strain in the cube. The other two side walls were constrained to deform only along the axis of the displacement; thereby resulting in a uniaxial strain state. The design, meshing and loading conditions can be found in Figure 3.8.
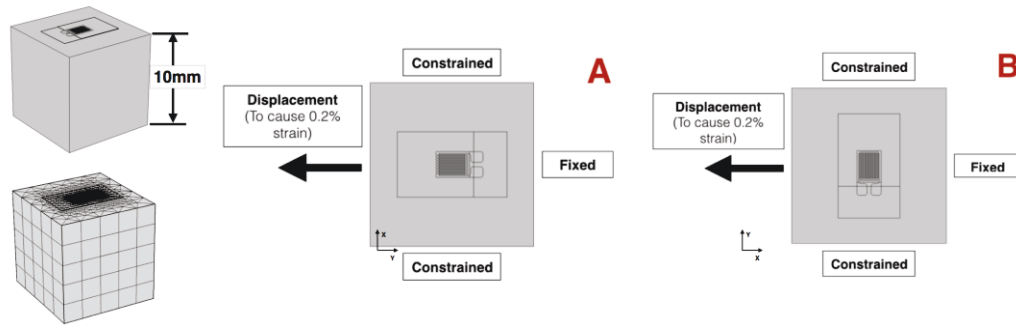
Figure 3.8: (Left) cube model geometry and mesh. (Right) top view of axial (A) and transverse (B) cube model loading conditions and constraints

3.3.2 Results

Table 3.6: Axial uniaxial cube model results (in tension) and comparison to analytical GF

Strain				Resistance	Axial Gauge Factor	
Target Axial	Y-dir	X-dir	Z-dir	R0 = 120.67	GF COMSOL	GF Analytical
0.002	0.0020	0.0000	-0.0009	121.03	1.665	
0.016	0.016	0.0000	-0.0075	123.88	1.665	**1.654**
0.03	0.0305	0.0000	-0.0140	126.76	1.665	

Table 3.7: Transverse uniaxial cube model results (in compression) and comparison to analytical GF

Strain in Tension				Resistance	Transverse Gauge Factor	
Target Transverse	Y-dir	X-dir	Z-dir	R0 = 120.67	GF COMSOL	GF Analytical
-0.002	0.0000	-0.0020	0.0005	120.68	-0.021	
-0.016	0.0000	-0.0159	0.0041	120.71	-0.020	**-1**
-0.03	0.0000	-0.0295	0.0075	120.74	-0.020	

Table 3.8: Transverse uniaxial cube model (in tension) results and comparison to analytical GF

Strain in Compression				Resistance	Transverse Gauge Factor	
Target Transverse	Y-dir	X-dir	Z-dir	R0 = 120.67	GF COMSOL	GF Analytical
0.002	0.0000	0.0020	-0.0005	120.66	-0.040	
0.016	0.0000	0.0161	-0.0041	120.62	-0.024	**-1**
0.03	0.0000	0.0305	-0.0078	120.59	-0.022	

These results (Tables 3.6 to 3.8) show that the strain gauge is responsive to strain applied in the primary axis of the strain gauge and that the gauge factors from COMSOL match the gauge factors derived in the analytical model. However, when strain is applied in the transverse direction, the strain does not deform the strain gauge as much as is theoretically expected and as such, the change in resistance when strain is applied perpendicular to the primary axis of the strain gauge is negligible.

3.4 Discussion

Looking at the models for the geometric change in resistance (Sections 3.2and 3.3), it can be said, that when strain is applied in the primary axis of the strain gauge, there is a noticeable change in resistance. The change in resistance from the models is directly proportional to the

strain applied and as such, produces a relatively constant gauge factor that is within 0.5% of the gauge factor derived from the analytical model.

However, when the applied strain is acting perpendicular to the primary axis of the strain gauge, the transverse strain is not properly transferred to the strain gauge grids and as such, is incapable of causing a noticeable change in resistance. The reason for this can be allocated to the difference in stiffness between substrate and strain gauge as well as the amount of shared boundary for the strain transfer.

3.4.1 Strain Transfer Theory

The steel tensile coupon is stiffer (higher Young's modulus) than the polyimide substrate and as such, all of the substrate's bottom surface area is in contact with the steel surface; hence, there is complete transfer of strain from the steel coupon to the polyimide substrate. However, the polyimide is less stiff than the constantan strain gauge and in addition to this, the contact surface area of the strain gauge's grids is relatively smaller. It is believed that this affects the strain transfer mechanism in two ways; firstly, due to its lower stiffness, the polyimide cannot completely transfer strain to the strain gauge without losing some of that strain during the transfer. Secondly, without a sufficient shared boundary between the polyimide and strain gauge, there can be no proper strain transfer.
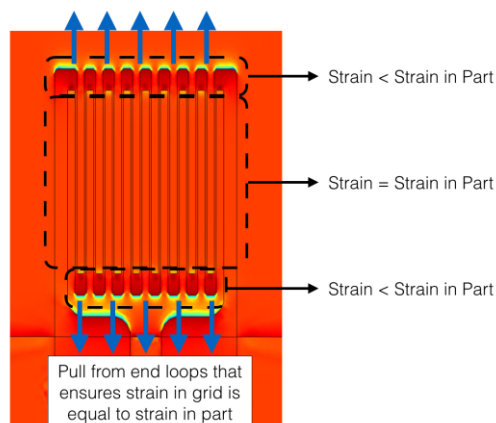
Figure 3.9: Schematic explaining strain distribution in axially mounted model

Revisiting the strain field of the axially mounted strain gauge, it can be observed that there are strain losses in the end loops that make the right strain in the grids possible (Figure 3.9). Since the grids are accountable for majority (>95%) of the change in resistance, the axially mounted model can lose strain in the end loops and still have an accurate gauge factor.

In the case of the strain gauge mounted transversely, the end loops are not oriented in a way that supports transverse strain transfer and as such, strain transfer to the strain gauge is poor as shown in Figure 3.7.

3.4.2 Validating Stiffness Hypothesis

To test the stiffness hypothesis, the stiffness of the polyimide substrate in both the axially and transversely mounted models was increased to match that of the constantan strain gauge. The models were run and the results (Figure 3.10) show that, with the substrate being as stiff as the strain gauge, there is proper transfer of strain to the strain gauge grids in both the axially and transversely mounted models.
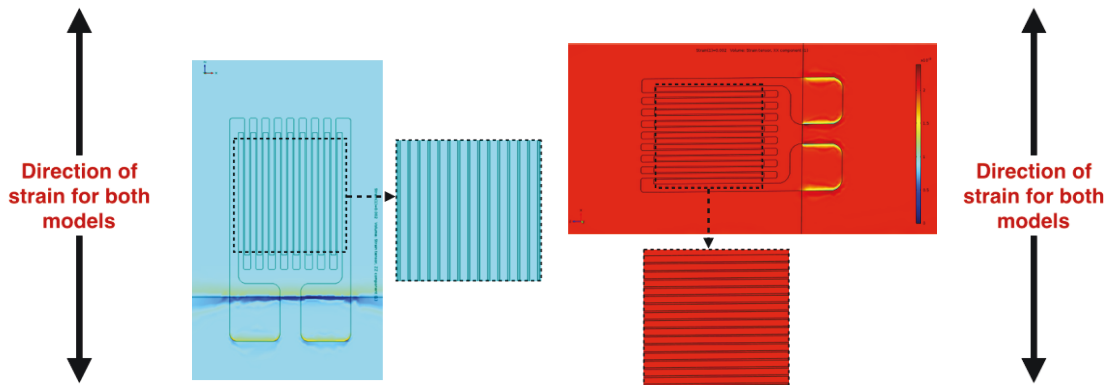
Figure 3.10: Strain distribution in axially (left) and transversely (right) mounted models with polyimide substrate being as stiff as strain gauge

On taking the change in resistance and solving for the gauge factors, it was observed that the gauge factor for the axially mounted model still matched the gauge factors shown in Table 3.2. However, for the transversely mounted model, the magnitude of the gauge factor increased from **-0.473** to **-0.863**, which is closer to the analytically derived value of -1.

34

3.4.3 Practical Meaning of Results

This means that strain gauges printed on kapton will act differently from strain gauges printed on stiffer substrates when there is strain that is not acting along the primary axis of the strain gauge.

In a uniaxial loading condition, the stiffness effect be noticeable when dealing with a stiff part that has a poisson's ratio higher than that of the strain gauge. If the cross-sectional shrinkage of the strain gauge grids exceeds the surface transverse shrinkage of the stiffer part under the strain gauge then the change in resistance remains predictable because the gauge factor accounts for the shrinkage of the strain gauge grids. However, if the part shrinks more than the strain gauge grid (due to a higher poisson's ratio) then there is an additional transverse strain being transferred to the strain gauge. Moreover, if the part under the strain gauge is stiffer than the strain gauge material then this additional transverse strain will be transferred to the strain gauge and the gauge factor will be affected.

In the case of biaxial loading of a stiffer part with a strain gauge printed directly on the part, the effects of the transverse strain should be accounted for; either by using two strain gauges perpendicular to each other or by introducing a less stiff medium between the strain gauge and the part to hinder the transfer of transverse strains to the strain gauge grids.

3.4.4 Introducing Piezoresistive Correction Factor, C_{pz}

So far, the derived gauge factors represent the geometric gauge factor; however, the actual or total gauge factor of a conventional strain gauge is ~2.05. The piezoresistive change in resistance is believed to be caused by deformation (or strain) of the crystalline lattice structure [34] and, for the range of deformation being explored in this thesis, this change in resistance is linear [34]. The geometric change in resistance is also linearly proportional to strain. Therefore, the piezoresistive change in resistance can be made proportional to the geometric change in resistance and the total change in resistance can be made proportional to the geometric change in resistance. The same concept can be applied to the gauge factors as follows:

$$\Delta R_{geometric} = \varepsilon_l (1 + 2v)R \qquad\qquad \to \Delta R_{geometric} \propto \varepsilon_l$$

Recall, $d\rho \propto \varepsilon_l$ and $\Delta R_{piezoresitive} = \left(\frac{d\rho}{\rho}\right)R \qquad \to \Delta R_{piezoresitive} \propto \varepsilon_l$

$$\therefore \Delta R_{geometric} \propto \Delta R_{piezoresitive} \qquad \to \Delta R_{piezoresitive} = C_1.\Delta R_{geometric}$$

$$\Delta R_{total} = \Delta R_{geometric} + \Delta R_{piezoresitive} \qquad \to \Delta R_{total} = (1 + C_1)\Delta R_{geometric}$$

Recall, $GF \propto \Delta R \qquad \to GF = C_2.\Delta R$ and $\Delta R = C_3.GF$

$$\therefore GF_{total} = C_2\Delta R_{total} = C_2(1 + C_1)\Delta R_{geometric} = C_2(1 + C_1)C_3 GF_{geometric}$$

$$\to \boldsymbol{GF_{total} = C_{pz}GF_{geometric}}$$

With $GF_{total} = 2.075$ and $GF_{geometric} = 1.66$, C_{pz}, for a conventional constantan strain gauge can be calculated as $GF_{total}/GF_{geometric} \qquad \to \boldsymbol{C_{pz} = 1.25}$

This means that the piezoresistive change in resistance accounts for 25% of the total change in resistance.

3.5 Validation of COMSOL Model and Derived C_{pz}

3.5.1 Transverse Sensitivity

The transverse sensitivity of a strain gauge is a measure of the strain gauge's response to strain acting perpendicular to the primary axis of the strain gauge (i.e. transverse strain). Transverse sensitivity can introduce errors into strain readings if the transverse sensitivity of the strain gauge is high and the strain gauge is used in a multi-axial strain field. A common example of this is using a strain gauge to sense strain on a tensile coupon during a uniaxial tensile pull. The cross-sectional area of the tensile coupon will shrink based on the poisson's ratio of the tensile coupon; thereby, creating a biaxial strain field. As discussed in Section 3.4.3, the transverse sensitivity of a strain gauge can be neglected if the transverse strain on the strain gauge is lower than the shrinkage strain on the strain gauge grids. In other words,

if the poisson's ratio of the strain gauge material is higher than the poisson's ratio of the tensile coupon then the cross-sectional area of strain gauge grids will experience more shrinkage strain than the transverse shrinkage strain from the coupon and as such, not add additional strain to the strain gauge.

The effects and induced errors from transverse sensitivity is discussed in detail in ref. [39]. Transverse sensitivity is mostly considered when the strain gauge is being used in a uniaxial stress field that results in a biaxial strain field with transverse strain, $\varepsilon_2 = -v\varepsilon_1$. Since ε_2 is negative (in comparison to ε_1) it increases the change in resistance and, inherently, the gauge factor. For example; consider a strain gauge mounted axially on a tensile coupon. When the tensile coupon is pulled, the grids of the strain gauge are subjected to tension and become elongated. Assuming the poisson's ratio of the tensile coupon is higher than that of the strain gauge, the tensile coupon will have a significant shrinkage in the cross-sectional area. This shrinkage will introduce a strain, ε_2, on the strain gauge grid that compresses the width of the strain gauge grids and this compression in grid width will cause an additional increase in strain gauge resistance.

Hence, strain gauge manufacturers will define transverse sensitivity as a percent increase in gauge factor (Figure 3.11).

Figure 3.11: EA-06-062AP-120/E strain gauge from micro-measurements highlighting transverse sensitivity value
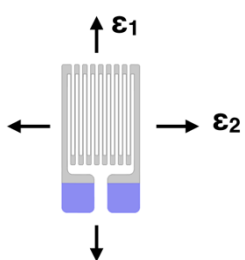
Validation of all the work that has been so far can be done by comparing the transverse sensitivity from the models to the manufacturer prescribed transverse sensitivity in Figure 3.11. A transverse sensitivity of 1.1 to 1.5% for a strain gauge with a gauge factor of 2.075 means that the effects of transverse strain will increase the gauge factor by **0.023** to **0.031**.

Validating the model and derived piezoresistive factor can be done in two ways:

1. Looking at the transverse model in Section 3.2 and determining how much change in gauge factor was introduced due to transverse sensitivity
2. Looking at the gauge factors of the transverse uniaxial strain cube models in Section 3.3

3.5.2 Validation via Transverse Model in Section 3.2

In the model described in Section 3.2, the poisson's ratio of the constantan strain gauge is higher than that of the steel tensile coupon and as such, the effect of transverse sensitivity can be neglected for the axially mounted strain gauges. However, for the transversely mounted strain gauges, the transverse strain is the primary strain and this means that the transverse strain is significant. In an ideal uniaxial loading scenario, the axial gauge factor can be related to the transverse gauge factor as follows:

$$GF = \frac{\Delta R}{R\varepsilon_1} \quad \text{and} \quad GF_t = \frac{\Delta R}{R\varepsilon_2}$$

In a uniaxial stress state; $\varepsilon_2 = -v\varepsilon_1$

Hence; $GF_t = \frac{-v\Delta R}{R\varepsilon_1} = -vGF \quad \text{or} \quad GF = -GF_t/v$

This means, without errors from transverse sensitivity, the transverse model in Section 3.2 should have a transverse gauge factor of -0.285(1.66) = **-0.473**. However, the transverse gauge factor of the transverse model in compression produced a median value of **-0.483**.

Converting this to the axial gauge factor and applying the piezoresistive correction factor of 1.25: $GF\ (with\ transverse\ sensitivity) = \left(-\frac{-0.483}{0.285}\right)(1.25) = 2.118$

Subtracting this from the expected gauge factor of 2.075 results in a gauge factor increase of **0.043**, which is outside the stated transverse sensitivity gauge factor increase range of **0.023** to **0.031**. The gauge factor increase being outside the manufacturer specified range is believed to be due to rounding errors and precision of the model. Based on the results in Table 3.5, the accuracy model to the third decimal place is in question and by merely changing the attained transverse gauge factor from -0.483 to -0.480 the gauge factor increase falls in the prescribed range. Therefore, it can be said that this result is acceptable.

3.5.3 Uniaxial Strain Cube Model in Section 3.3

The transverse uniaxial strain cube model focuses primarily on understanding the transverse sensitivity by directly measuring the change in gauge factor caused by only transverse strain. Table 3.7 shows the geometric change in gauge factor when the strain gauge is only compressed in the transverse direction. This is equivalent to measuring the effects of the cross-sectional shrinkage of a tensile coupon without including the elongation of the strain gauge grids. Table 3.7 shows that the geometric gauge factor from only transverse loading is **-0.020**. The negative value entails that the strain gauge resistance will drop when the strain gauge is exposed to a positive strain (tension) in the transverse direction and vice versa. Applying the piezoresistive correction factor of 1.25 to this value results in a gauge factor of **-0.025**. This means that, in the uniaxial loading of a tensile coupon with significant cross-sectional shrinkage (transverse compression), the transverse compression will increase the gauge factor by **0.025** and this value falls within the manufacturer's specified gauge factor increase range; thereby, validating the model.

3.6   Chapter 3 Summary

Chapter 3 focused on modeling the strain gauge performance and validating the models developed. An analytical and numerical model were developed. The analytical model used a partial differential method to analyze the change in resistance of a single wire modeled as a rectangular prism. The analytical model resulted in an equation that broke the change in resistance of a strain gauge into a geometric and a piezoresistive component.

The analytical model was followed by numerical models developed with COMSOL, which comprised of two tensile coupons; whereby one model had a strain gauge mounted in the axial orientation and the other model had the strain gauge mounted in the transverse orientation. The results of the models showed that the axially oriented strain gauge matched the analytical model, while the transversely oriented strain gauge showed a loss in transverse strain transfer that required further investigation.

The loss in transverse strain transfer was investigated and confirmed with a uniaxial strain state cube model. The discussion following this model stated that there is a loss of transverse strain in softer or less stiff substrates and that special care should be taken when dealing with high transverse strains on stiffer substrates.

The results from the axially oriented models were used to derive a piezoresistive correction factor, which was validated, alongside the model, by comparing the transverse sensitivity from the models to the actual transverse sensitivity prescribed by the strain gauge manufacturer.

CHAPTER 4

4 EXPERIMENTS

4.1 Printing Procedure
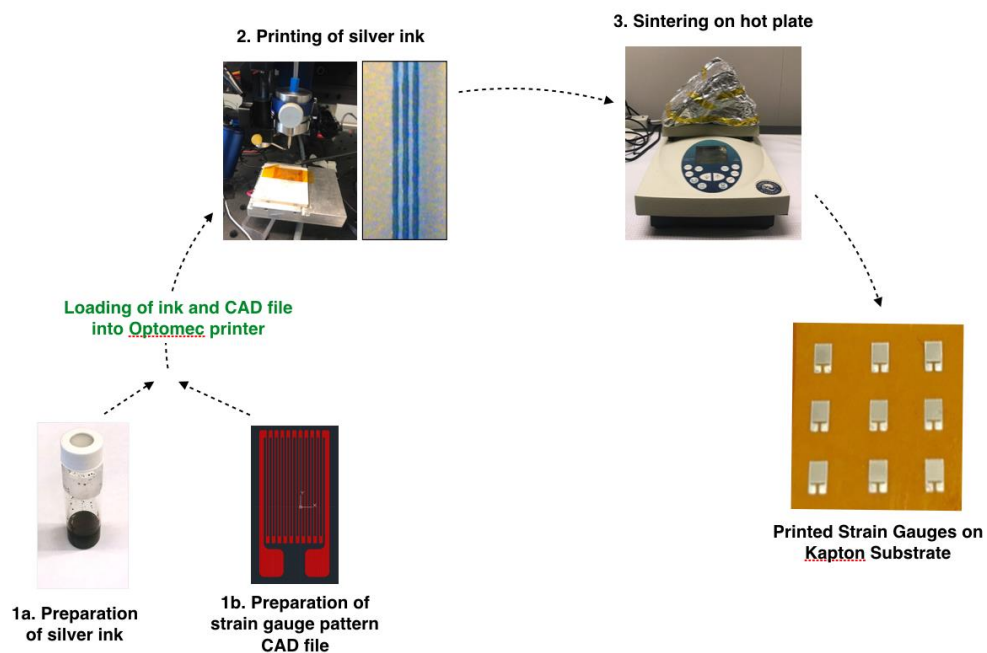
Figure 4.1: Schematic for printing a strain gauge from silver ink

Figure 4.1 summarizes all the steps required to print a strain gauge using silver ink. The detailed procedure is as follows:

1. Preliminary preparations need to be made. The ink as well as the strain gauge pattern need to be prepared.

- The ink used in this thesis is a silver nanoparticle ink from NovaCentrix. Research was carried out on several silver inks from several vendors before choosing this ink. For this thesis, the ink is diluted in distilled water at a 1:2 ratio, with 1.5cc of water to 3cc of the ink. The mixture is done in a vial and then placed in a sonification bath afterwards to ensure that there are no agglomerated silver nanoparticles before printing. The mixture is also placed on a vortex mixer to ensure proper mixing and dispersion of the silver nanoparticles. After this is done, the vial containing the mixture is placed in the ultrasonic atomizer chamber by using a sleeve to hold the vial in place.

- The CAD file for the strain gauge pattern is prepared using AutoCAD. For this thesis, the CAD file was modified to print two additional layers on the strain gauge grids to guarantee that there was enough material in the grids and prevent cracks in the grids after sintering. A crack in the grid renders the printed strain gauge unusable either by making it non-conductive or by making it have a non-linear response to strain. After the AutoCAD .dxf file is created, it is exported as a vector-path program file using an M^3D extension that is compatible with AutoCAD. The program file is then imported into the printer's control system and an origin is set; thus, completing pre-printing setup.

2. For the printing process, process parameters need to be set and each process parameter influences the material deposition from the nozzle. The process parameters and their effects are as follows:

    - Atomizer Power (Units: Volts): The atomizer power affects the amplitude and frequency of the ultrasonic atomizer, which in turn affects how much vapor or aerosol is formed in the vial during the atomizing process. A higher atomizer power will result in more vapor being formed and vice versa. However, if too much vapor is formed then this could clog the nozzle as the

material tries to exit the nozzle. The typical range of this parameter is **35 to 45V** with the maximum attainable value being 50V.

- Atomizer Flowrate (Units: cc/min): The atomizer flowrate controls the flowrate of the atomizer gas that is used to carry the aerosol from the vial in the ultrasonic atomizer to the nozzle. The higher the flowrate the more material deposition and vice versa. This parameter depends on how much aerosol has been formed in the vial. If the aerosol in the vial is low, then this flowrate is increased to carry as much aerosol as possible; however, if the aerosol in the vial is high, then the flowrate is reduced to carry less aerosol so as not to clog the nozzle upon deposition. As such, the typical operating range of this parameter is quite broad with a range of **5 to 30cc/min**. The maximum attainable value is 200cc/min.

- Sheath Gas Flowrate (Units: cc/min): The sheath gas flowrate controls the flowrate of the sheath gas that is used to focus the aerosol stream. The sheath gas carries the aerosol from the tip of the nozzle to the substrate. Increasing the sheath gas flowrate can reduce the droplet diameter and increase resolution as shown in Figure 4.2. However, having a sheath gas flowrate that is too high can cause overspray, which is an excessively turbulent flow that leaves material outside the main material deposition line width as shown in Figure 4.3. The typical range of this parameter is **15 to 28cc/min**. The maximum attainable value is 200cc/min.

3. For this thesis, the sintering process is done on a hot plate. The substrate, with the printed sensor on it, is placed on a hot plate and heated to 280°C for 30mins. A foil housing or beaker is placed over the sensor, but the heating and cooling rates are not controlled. The sintering process evaporates the solvent and binders while forming sinter necks [21] between the silver nanoparticles to make the sensor conductive.
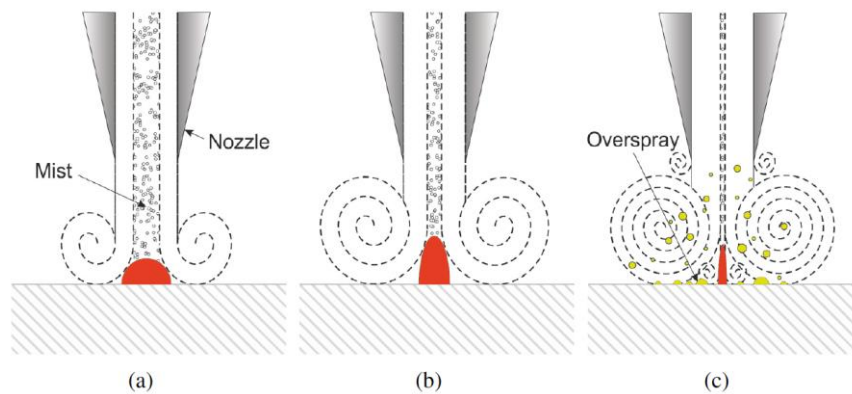
Figure 4.2: Schematics of different sheath gas flows (a) Low sheath gas flow (b) High sheath gas flow (c) Exceedingly high sheath gas flow [45]
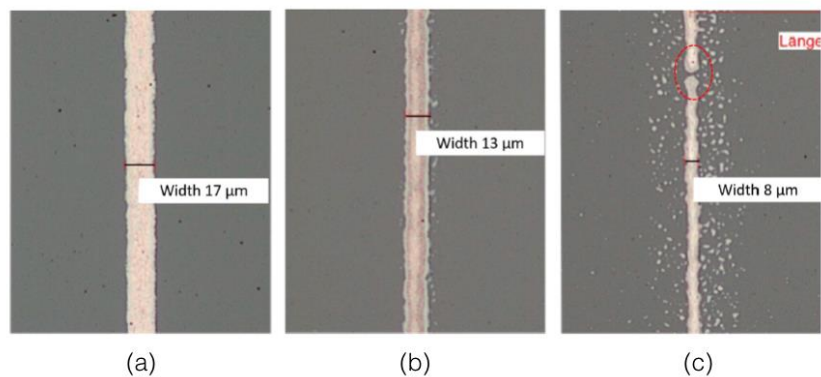
Figure 4.3: Microscope image of different sheath gas flows (a) Low sheath gas flow (b) High sheath gas flow (c) Exceedingly high sheath gas flow [45]

4.2 Characterisation of Printed Sensor

The result after sintering should be a conductive silver strain gauge comprising only of connected silver nanoparticles with a total strain gauge resistance in the range of 110 - 130Ω. Due to variations in the ink composition during printing, the final strain gauge resistance can fall outside the expected range even if the same printer parameters are being used.

Some of samples that fell within the acceptable resistance range were characterized using a VK-X laser scanning confocal microscope from Keyence. The images from the confocal microscope can be seen in
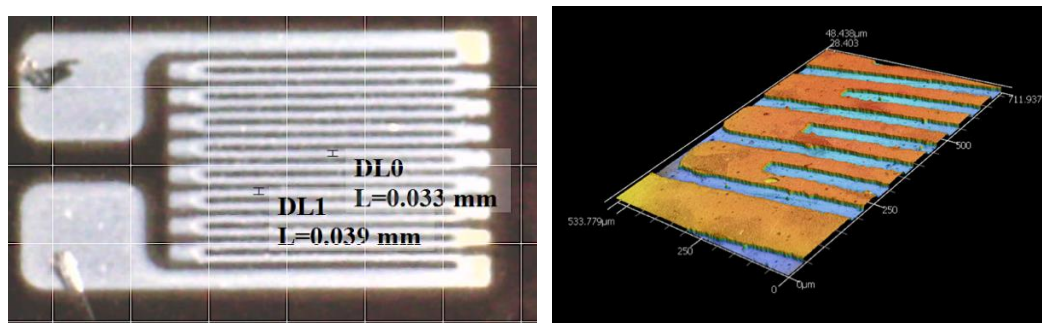
Figure 4.4: Image (left) and profile (right) of printed strain gauge on kapton substrate

The results from the confocal microscope show that, after sintering, the printed strain gauges have smooth features and the strain gauge grids take the shape of a rectangular prism with a width of 60μm and a height or thickness of 15μm. Further characterization showed that, to attain the ideal resistance of 120ohm, the width should be around 30μm and the height should be around 1μm (i.e. cross-sectional area of 30μm).

4.3 Printing Challenge and Attempted Solution

4.3.1 Challenges

One of the major challenges of printing the strain gauges was getting the strain gauges to fall within the target resistance of 110-130 ohms. Since the available strain gauge data acquisition equipment only worked with strain gauges within that range, it was imperative that the printed strain gauges fell within that resistance range. It was hoped that upon finding a set of printer process parameters that produced strain gauges in the right resistance range, the same set of parameters could be entered into the printer at any given time and the printed strain gauge would fall into the desirable resistance range.

However, it was observed that, due to minor variabilities in the ink composition or nozzle tip cleanness, the same set of parameters did not always produce the same strain gauge resistance. During the atomization process, it is believed that the aerosol consists of more solvent than silver nanoparticles and as such, overtime, the concentration of the ink changes, with the ratio of solvent to silver nanoparticles continuously dropping [40]. This change in ink concentration affects the atomization process by increasing or reducing the amount of aerosol being formed in the vial. A change in the amount of aerosol formed in the vial means that more or less material is carried to the nozzle by the atomizer flow gas and as such, more or less material is deposited onto the substrate, which then leads to a higher or lower strain gauge resistance after sintering.

4.3.2 Attempted Solutions

Since there is no real-time monitoring of the ink concentration, an attempt to monitor the material deposition using the attached optical camera was made. The plan was to take pictures of the printed grids and correlate that to the resistance after sintering. Table 4.1 shows an example of this plan being executed.

Table 4.1: (Left) Table showing images of printed grids and grids of strain gauges and attained resistance
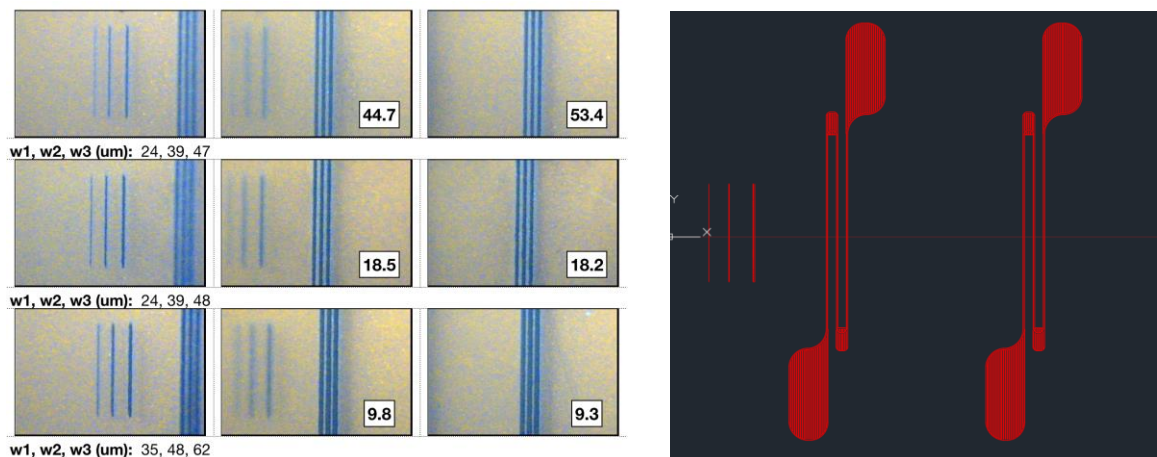
Figure 4.5: (Right) Strain Gauge Print Pattern for Resistance Study

For this study, three lines are printed with one layer, two layers, and three layers, respectively. A picture of this is taken and the widths of those lines are measured as w1, w2 and w3, respectively. The widths are measured from the image taken using a software called Image J, which takes measurements based on pixel count. As soon as the lines are printed, two strain gauges with only three grids each (Figure 4.5) are printed and, after sintering, their resistances are measured. In other to get a resistance of 120 ohms from a full strain gauge, the strain gauges with only three grids should have a resistance 22.5 ohms.

This study was indecisive as can be seen from the first two rows of Table 4.1, which have very similar line widths but significantly different resistances. The failure of this study can be allotted to the resolution of the camera and the inability to accurately measure the width of the lines.

Another attempt was made at getting the target resistance by monitoring the material deposition using an area, rather than width, measurement. For this study, a better camera is used to take a picture of six printed lines (two 2 layers, two 4 layers and two 6 layers as per Figure 4.6). The image is imported into Image J and converted into a binary (Figure 4.6); whereby the white pixels represent metal deposition and the black pixels represent the substrate. The average pixel intensity within a rectangular region is obtained as that correlates with the surface area of deposited material. As soon as the six lines are printed, two strain gauges with three grids are also printed, so as to have a resistance value to associate with the obtained average pixel intensity. This average pixel intensity is then plotted against resistance (Figure 4.7) to see if there is a correlation.

From the results in Figure 4.7 it can be said that there is a slight correlation between the material deposition area of the printed lines, which is represented here by the average pixel intensity within a rectangular region, and the resistance of the strain gauge after it has been sintered. From observation, it can be said that a higher material deposition area (represented here by a higher average pixel intensity) will result in a lower resistance. More experiments and a more in depth statistical analysis is required to fully understand and adapt this correlation into the strain gauge resistance optimization process.
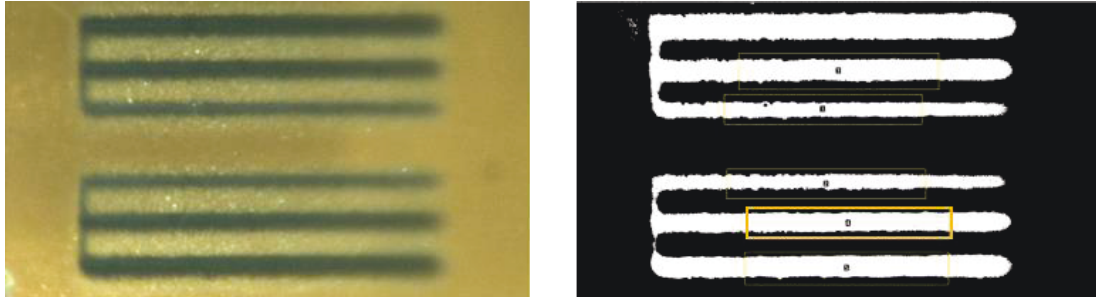
Figure 4.6: Image of six printed lines (Left). Image converted to binary and highlighting one of the regions for the average pixel intensity measurement (Right)
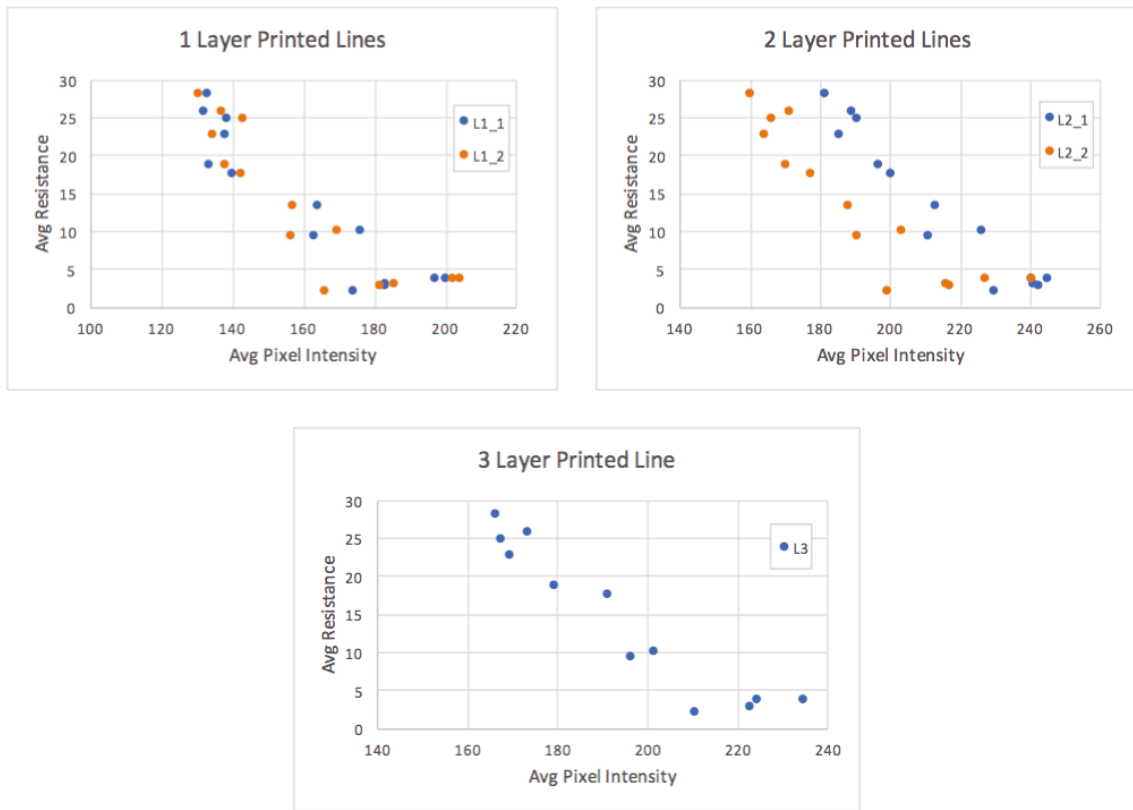
Figure 4.7: Results of printed line material deposition area (from average region pixel intensity) to resistance

4.4 Test Sample Preparation

For the experimental portion of this thesis, silver strain gauges were printed using the Optomec M^{3}D printer and tested. The strain gauges were printed using an ink that contains dispersed silver nanoparticles, which was purchased from Novacentrix. The ink was diluted in water at a 2:1 ink to water volume ratio. It had been discovered from previous experiments that diluting the ink leads to better printing. The strain gauge CAD pattern was created based on the model in Appendix B and used to print strain gauges with the geometry of conventional strain gauges. The strain gauges for testing and characterization were printed on two different types of substrate:

a. Kapton: The samples printed on kapton were meant for direct performance comparison to conventional strain gauges. The strain gauges were printed on a kapton film, sintered, and cut to size.

b. Coated Tensile Coupons: In order to print directly on a metallic part, an insulating layer or coating needs to put on the part before the strain gauge is printed. Tensile coupons made from aluminum were coated with an insulating alumina sol-gel [41] using a dip-coating process and silver strain gauges were printed directly on the coated coupons. Pores and cracks in the coating made samples printed on this substrate unusable.

Figure 4.8: (Left) Uncovered printed strain gauge showing strain gauge and silver solder on tensile coupon. (Right) Kapton tape placed over printed strain gauge for protection

The printed strain gauges did not respond well to high temperature soldering guns so, thin lead wires were attached to the printed strain gauges using a silver nanoparticle paste from NBE technologies that had to be sintered afterwards at a temperature of 260°C for 30mins. The solder can be seen in Figure 4.8. This assembly was then attached to a steel tensile coupon along with copper solder pads using the procedure described in ref. [17]. Kapton tape was placed over the strain gauge (Figure 4.8) to provide protection and encapsulation similar to conventional strain gauges. The thin lead wires were soldered to the copper solder pads and then thicker lead wires that connected to the DAQ were also soldered to the copper solder pads. The tensile coupons with the mounted and wired strain gauges were then subjected to tensile loading.

Some of the samples printed on kapton were also subjected to higher temperatures (25-75°C above room temperature) to determine the thermal response of the printed samples

Using a strain gauge DAQ, the strain being measured by the strain gauge was recorded and compared to either the calculated strain or to the strain being recorded by a conventional strain gauge.

4.5 Testing Equipment

After the strain gauges have been printed and sintered, and lead wires have been attached, the equipment required for testing are as listed:

1. Mark-10 manual tensile tester (Figure 4.9): Pulls the tensile coupon when the handle is rotated. Used for force value testing i.e. turning the handle to a certain force value and holding it at that force value to see the strain response

2. Instron model 4206 programmable tensile tester (Figure 4.9): Programed to pull the tensile coupon at a constant displacement rate. Used for plotting strain vs force or strain vs displacement curves

3. HG 2510 ESD programmable heat gun (Figure 4.9): Used for heating up the strain gauges and determining the thermal response
4. NI-9237 strain gauge data acquisition module: Reads strain data from strain gauges
5. EA-06-062AP-120/E conventional strain gauge for comparison

Figure 4.9: (Left) Manual hand-operated tensile tester, (middle) electric programmable tensile tester and (right) heat gun

4.6 Testing Procedure

After the samples were attached to the steel tensile coupons, the tensile coupon was subjected to tensile loading using the tensile testers machines mentioned in Section 4.5.

The manual tensile tester was used to test the printed strain gauges in steps and determine the total gauge factor of the printed sensor. This was done by loading the coupon to a specific tensile force and keeping that force fixed for short period to see the strain prediction from the strain gauge. The expected strain on the coupon was calculated or was determined by using a conventional strain gauge. The conventional strain gauge was either placed on the other side of the coupon that the printed strain gauge was attached to or it was placed on a

different coupon with the same geometry and made from the same material. The coupon was loaded to different tensile force values and the gauge factor of the printed strain gauge was varied until the strain from the printed strain gauge matched the expected strain or strain from the conventional strain gauge. The force values were stepped up to a maximum value of about 300kgf and then stepped down to 0 to see if there was any plastic or permanent deformation of the printed sensor during loading. Some of the tests were also carried out more than once to observe the repeatability of the printed sensors.

The programmable tensile tester was used to load the sample at a constant displacement rate of 2mm/min until a maximum force of about 300kgf was reached. For one sample, the printed strain gauge was loaded until the strain gauge failed and the failure strain was recorded.

Due to unforeseen changes in the material deposition during printing, the printed strain gauges varied in resistance after sintering. The resistance of each printed strain gauge was entered into the strain gauge DAQ to account for the varying resistance of each strain gauge and ensure that the calculated strain from the DAQ was accurate.

A total of 10 strain gauges were printed on kapton and attached to tensile coupons. Some of the strain gauges were mounted axially (primary axis of strain gauge is parallel to the primary strain direction) while others were mounted transversely (primary axis of strain gauge is perpendicular to the primary strain direction). Some of these samples had a conventional strain gauge attached to the other side of the tensile coupon for strain comparison. All the samples were loaded on the manual tensile tester for the step testing but only a select few were tested using the programmable tensile tester as well.

4 of the samples printed on kapton were subjected to thermal loading using the heat gun. During the thermal loading, no mechanical load was applied to the tensile coupon. The heat gun was placed close to the sample with hot air blowing directly on the sample. The heat gun was set to 50°C and held over the sample for 30-120seconds, depending on when it was assumed that the strain gauge had reached thermal equilibrium. Afterwards, the heat gun was

moved away from the sample, set to 100ºC and allowed to reach the newly set temperature before being held over the sample again. The plan was to subject the samples to temperatures up to 200ºC but, the temperature induced resistance change made the resistance of the samples outside the DAQ's operating resistance.

A summary of the features of each sample can be seen in Table 4.2.

Table 4.2: Summary of Tests Run

Sample ID	Substrate	Printed Strain Gauge Resistance (Ohms)	Gauge Factor Used	Mounting Orientation	Attached Conventional Strain Gauge	Additional Loading (other than manual tensile tester)	Number of Runs
1	Kapton	126	1.9	Axial	No	_	2
2	Kapton	110	1.8	Axial	No	Prog. Tensile tester	2
3	Kapton	125	2	Axial	No	Thermal	1
4	Kapton	111	1.4	Axial	No	_	2
5	Kapton	129	2.3	Axial	Yes	Prog. Tensile tester	1
6	Kapton	115	1.8	Axial	Yes	Prog. Tensile tester	1
7	Kapton	126	2.8	Axial	Yes	Thermal	1
8	Kapton	113	2.8	Transverse	Yes	Thermal and Prog. Tensile tester	2
9	Kapton	124	3	Transverse	Yes	Prog. Tensile tester	1
10	Kapton	119	6	Transverse	No	Thermal	2

4.7 Results and Discussion

4.7.1 Manual Tensile Tester Results

Conventional (Standard) Strain Gauge
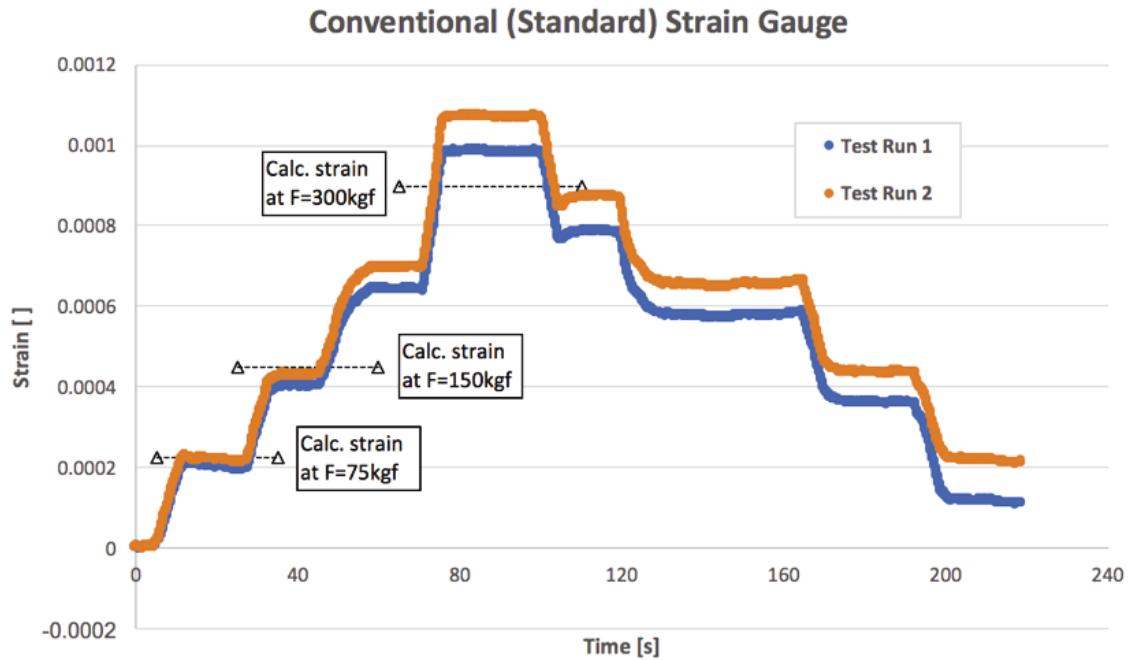
Figure 4.10: Conventional strain gauge run twice and showing calculated strain at specific loads

The calculated strain is derived from the applied force by using the linear relation between applied force and strain:

$\rightarrow$ $Stress, \sigma = Young's modulus, E \times Strain, \varepsilon$

$\rightarrow$ $\varepsilon = \sigma/E$ $\rightarrow$ $\varepsilon = F/(A \times E)$ (4.1)

$\rightarrow$ $where, F$ is applied force and A is the cross sectional area of the coupon
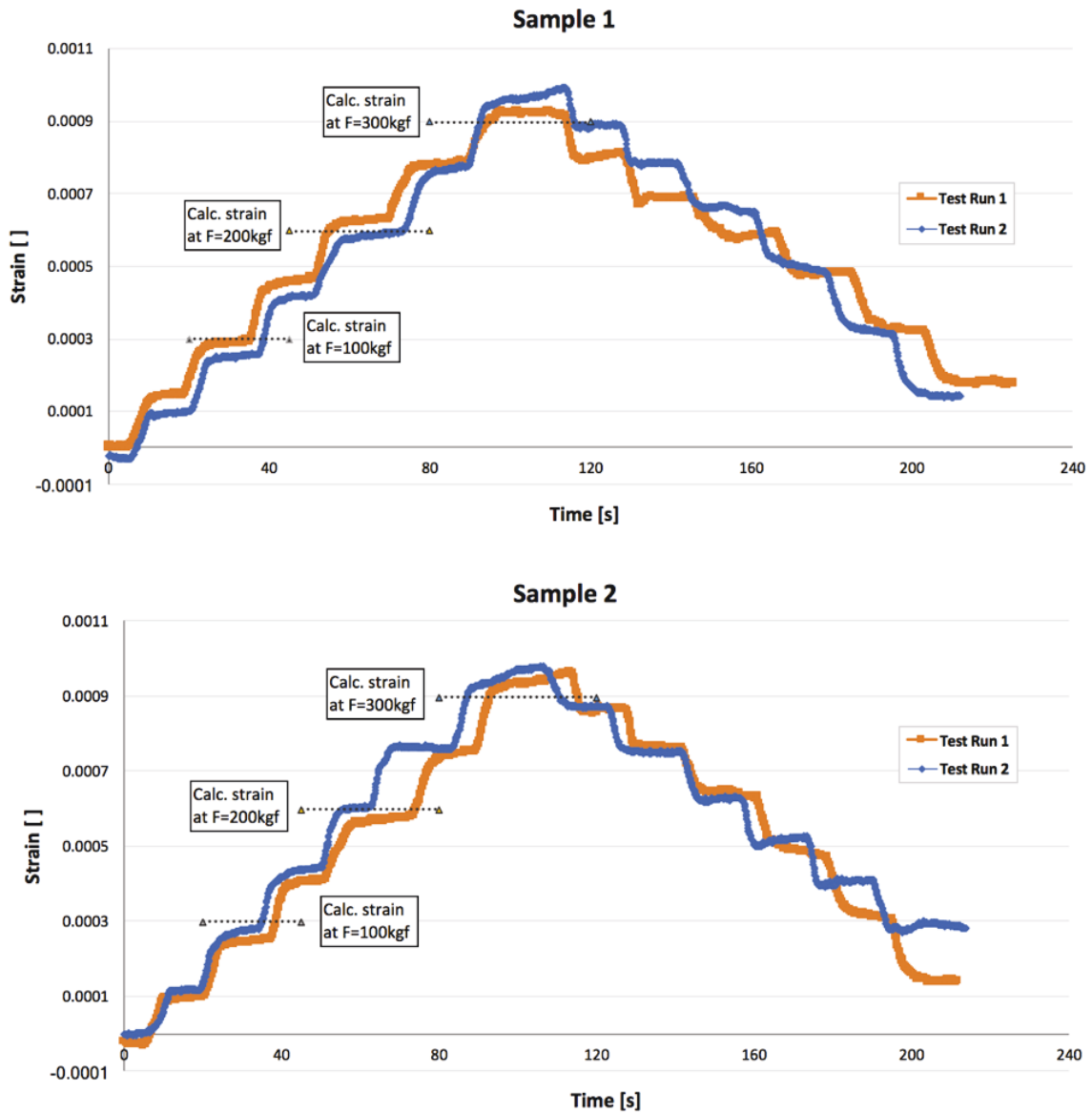
Figure 4.11: Samples 1 and 2 run twice and showing calculated strain at specific loads

The results in Section 4.7.1 show that the printed strain gauges have the potential to accurately detect strain, but the technology still requires some optimization. The experiment in Figure 4.10, which is done with a standard strain gauge shows that there may be errors in the experiment. The standard strain gauge is supposed to be accurate and the experiment is supposed to end at a force of 0kgf, which should result in a strain of 0. However, from the

experiment in Figure 4.10, it can be seen that the final strain is not 0, which could either be an indication of force reading errors in the manual tensile tester or an indication of plastic deformation in the tensile coupon. Since the strain can be zeroed at the start of each experiment, this error does not greatly affect future experiments. It only entails that a strain gauge could be preloaded before an experiment is begun. Overlooking this error, it can be said that the calculated strain matches the strain readings from the standard strain gauge up until the maximum force of 300kgf is applied and possible plastic deformation is introduced.

Figure 4.11 shows that, with the right gauge factor applied, the strain from the printed strain gauges can match the expected or calculated strain. It also shows that the printed strain gauges can be successfully used for up to two runs. More than two runs were not attempted on any of the samples and it should be noted that the strain value was zeroed at the start of each run. The samples in Figure 4.11 showed that the strain gauges did not read a strain value of 0 at the end of the experiment where the force is 0kgf; however, this is believed to be due to errors in the tensile tester or plastic deformation in the tensile coupon. Although it was not expected that the steel 1018 tensile coupon would plastically deform at such a low strain of 0.1%, it is a valid explanation for the phenomenon that was observed.

Figure 4.12 shows that the selecting the right gauge factor for the printed strain gauges is important when trying to get accurate strain readings. For this thesis, all the printed strain gauges did not have the same gauge factor and the right gauge factor had to be derived by comparison to calculated values or values from the standard strain gauge. This gauge factor issue can, however, be solved with proper process optimization.

Figure 4.13 shows a sample that has been run twice and is being compared to the standard strain gauge results. Since the printed and standard strain gauges were run on different tensile coupons at different times, some human and material errors were expected. However, based on observations from Figure 4.12 and Figure 4.13, it can be said that the strain readings from the printed strain gauges match the strain readings from the standard strain gauge to a certain level of accuracy. The discrepancies between test runs are believed to be a result of human error and errors from the manual tensile tester.

Sample 3: Varying Gauge Factors
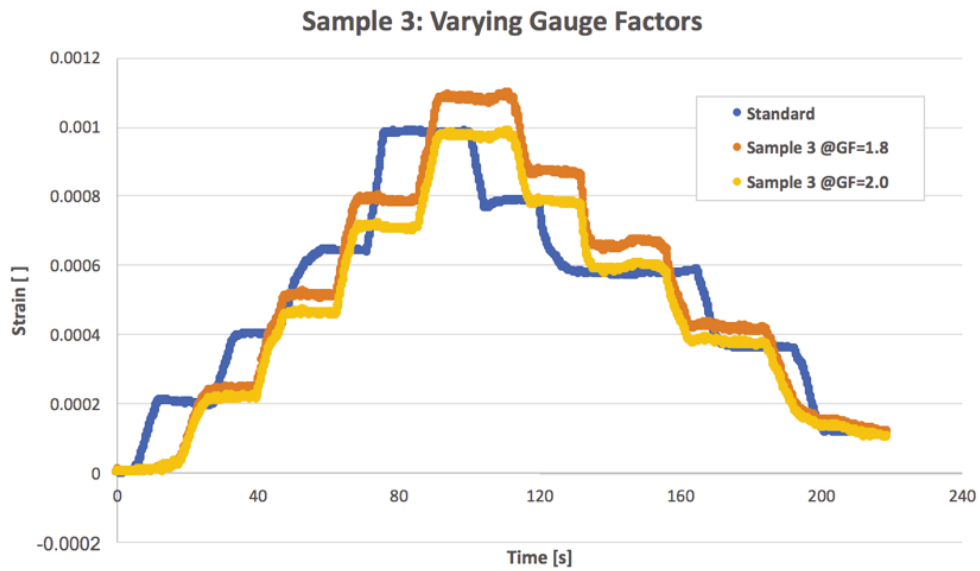
Figure 4.12: Sample 3 calculated with different gauge factors and being compared to the standard strain gauge result
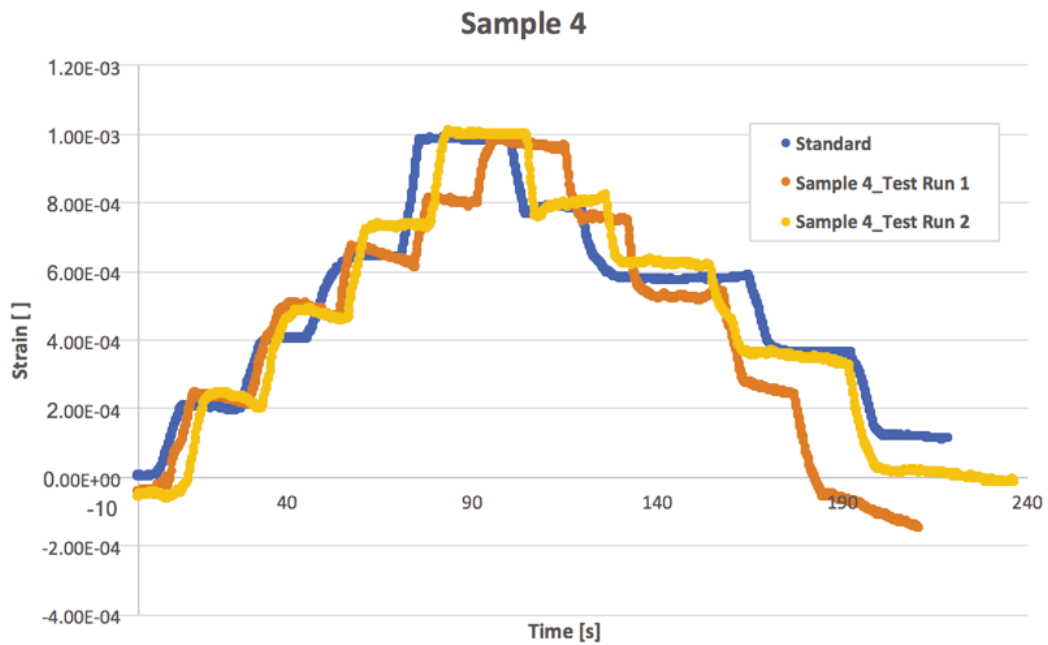
Sample 4

Figure 4.13: Sample 4 run twice and being compared to the standard strain gauge result

NOTE: For the following tests, the maximum force is 225kgf and not 300kgf
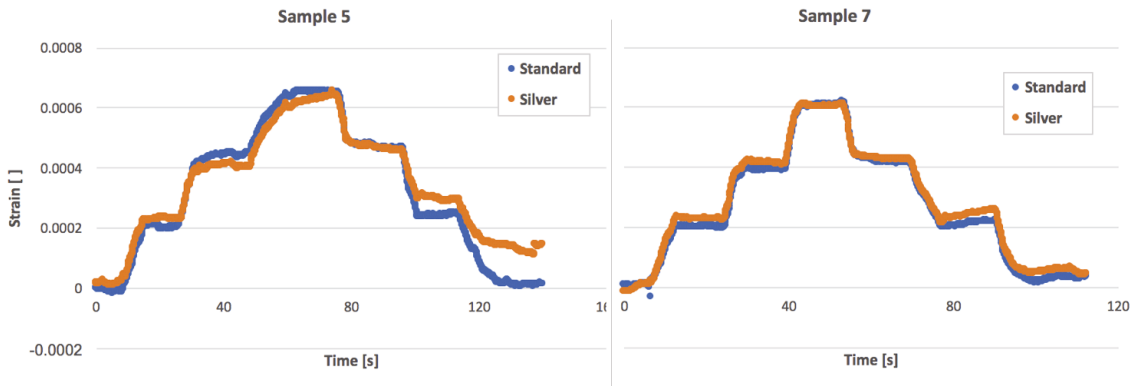
Figure 4.14: Samples 5 and 7 being compared to a standard strain gauge that was mounted on the other side of the tensile coupon
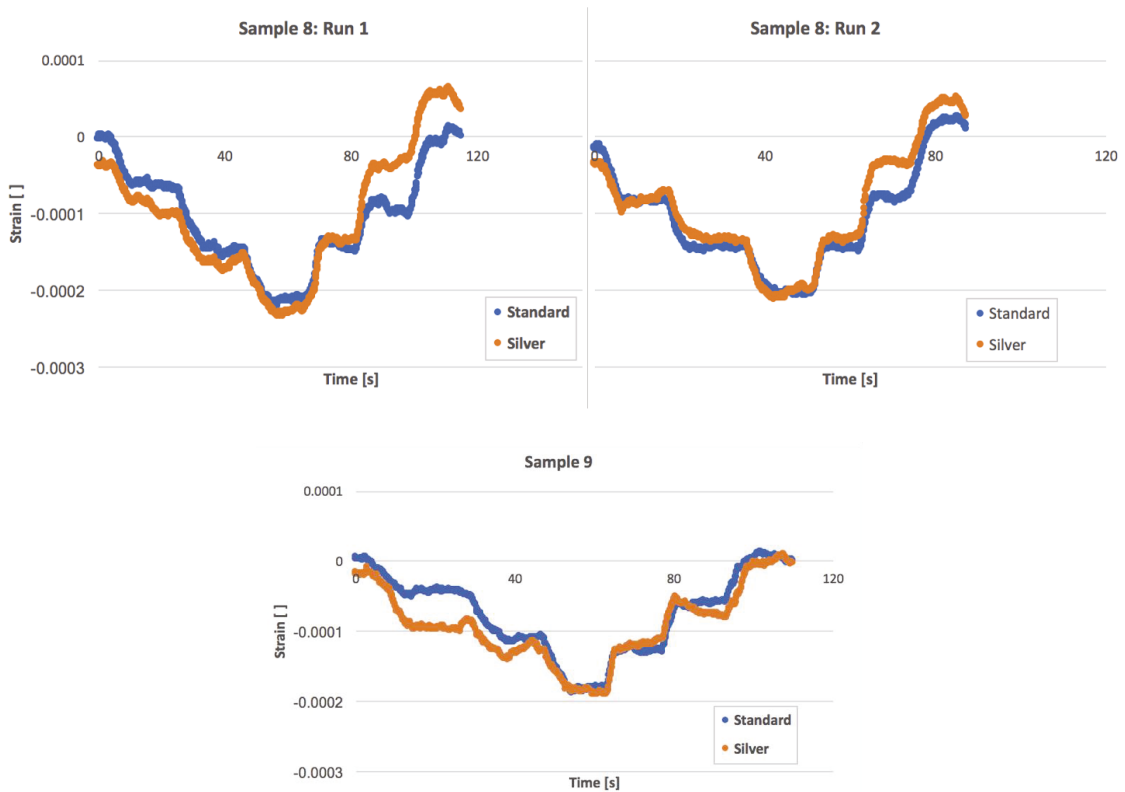
Figure 4.15: (Top) Sample 8 run twice while being compared to a standard strain gauge mounted on the other side of the tensile coupon. (Bottom) Sample 9 being compared to a standard strain gauge mounted on the other side of the tensile coupon

For samples 5 to 9, the maximum load applied by the manual tensile tester was reduced from 300kgf to 225kgf. This was done to try and eliminate any plastic deformation of the tensile coupon that was initially being introduced. The number of steps are also reduced from four to three and a standard strain gauge is attached to the other side of the tensile coupon. Data was simultaneously collected from the standard and printed strain gauges. Figure 4.14 shows that the printed strain gauge readings match the standard strain gauge readings very well with some discrepancy at the end of sample 5. There is currently no explanation for this discrepancy.

Figure 4.15 also shows the strain gauges that were mounted transversely and these results are also promising, with the printed strain gauges matching the standard strain gauges even after two runs (sample 8). However, there are still unexplainable discrepancies in certain locations of these results that need to be investigated further. It is important to note that the transversely mounted strain results in Figure 4.15 match the predictions from the model. The tensile coupon for samples 8 and 9 are subjected to the same loading history as samples 5 to 7 and the strain reading from samples 8 and 9 are very close to the expected tensile coupon poisson's ration shrinkage, i.e. transverse strain gauge strain reading = poisson's ration × axial strain gauge strain reading. In other words, the transversely mounted strain gauges only record the strain acting in the primary axis of the strain gauge with negligible effects from the strain acting perpendicularly to the primary axis.

Figure 4.16 shows sample 5 being loaded on the programmable tensile tester and the strain reading from the printed strain gauge does not match the strain reading from the standard strain gauge as well as the manual tensile tester experiment in Figure 4.14. At the end of this test run there is a 14% strain reading error between the printed and standard strain readings. It is possible, that at the start of this experiment, something may have happened to the printed strain gauge that changed the gauge factor. At the start of the experiment (around the 1 second mark), there appears to be a sudden jump in strain reading that affected the printed silver strain gauge more than it affected the standard strain gauge. Whatever caused this jump could be the cause of the error between the printed and standard strain gauge readings.

4.7.2 Programmable Tensile Tester Results
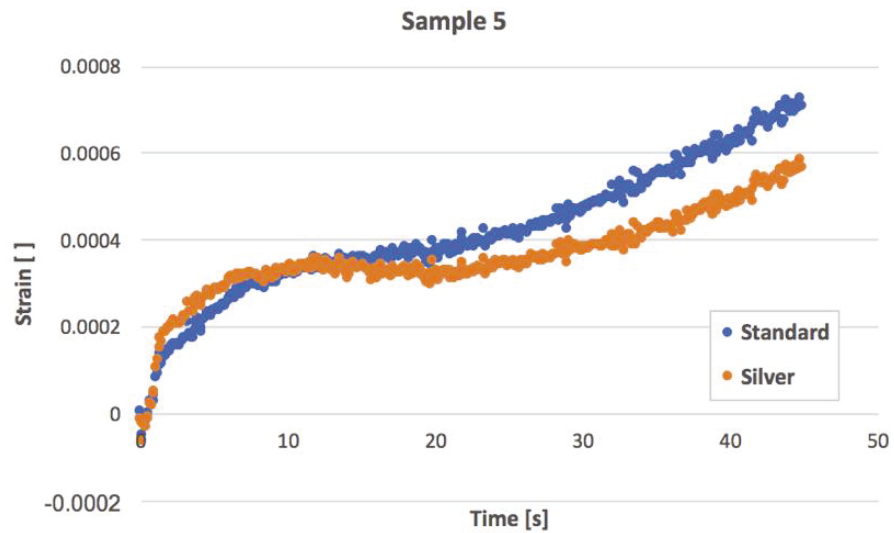
Figure 4.16: Sample 5 being compared to a standard strain gauge mounted on the other side of the tensile coupon
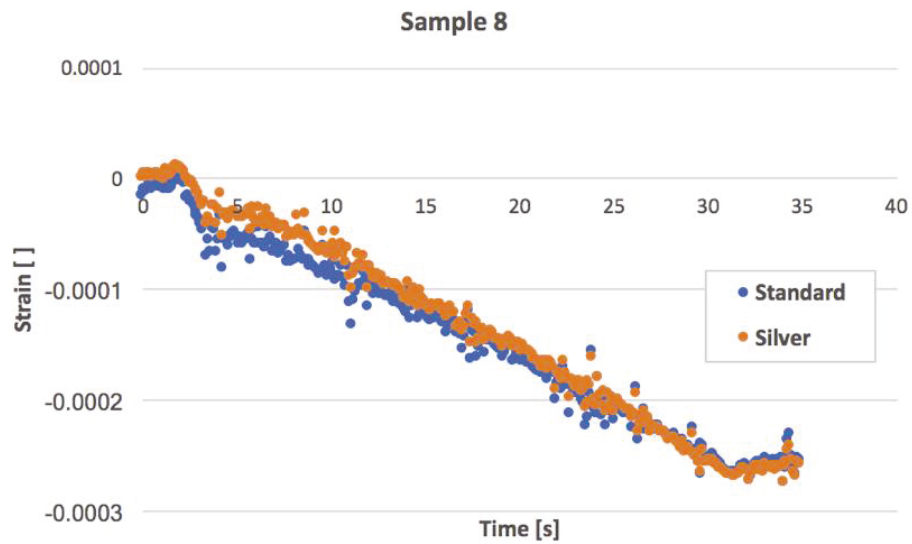
Figure 4.17: Sample 8 being compared to a standard strain gauge mounted on the other side of the tensile coupon

On the other hand, Figure 4.17 shows a promising result with the printed and standard strain readings matching very closely.

Looking at the properties of silver in ref. [42], the gauge factor of silver was calculated from that paper to be around 2.88 at low strains (~1%) and around 1.6 at higher strain (~10%). Most of the printed samples were tested at low strains and have a gauge factor in the range of 1.4 to 3, with one sample having a gauge factor of 6. Although these gauge factors are comparable to the results in literature, it is an indication that there are events in the printing process that are influencing the gauge factor and making it vary.

4.7.3 Test to Failure

Figure 4.18 shows sample 2 being loaded until the strain gauge failed. The failure strain is ~1.6%, which is about half the failure strain of a conventional strain gauge [35]. The strain in the elastic region is also calculated from the force and plotted to see how well the printed strain gauge correlates with that. From the zoomed in view, it appears that the measured strain from the printed strain gauge is very close (within 5%) to the calculated strain.
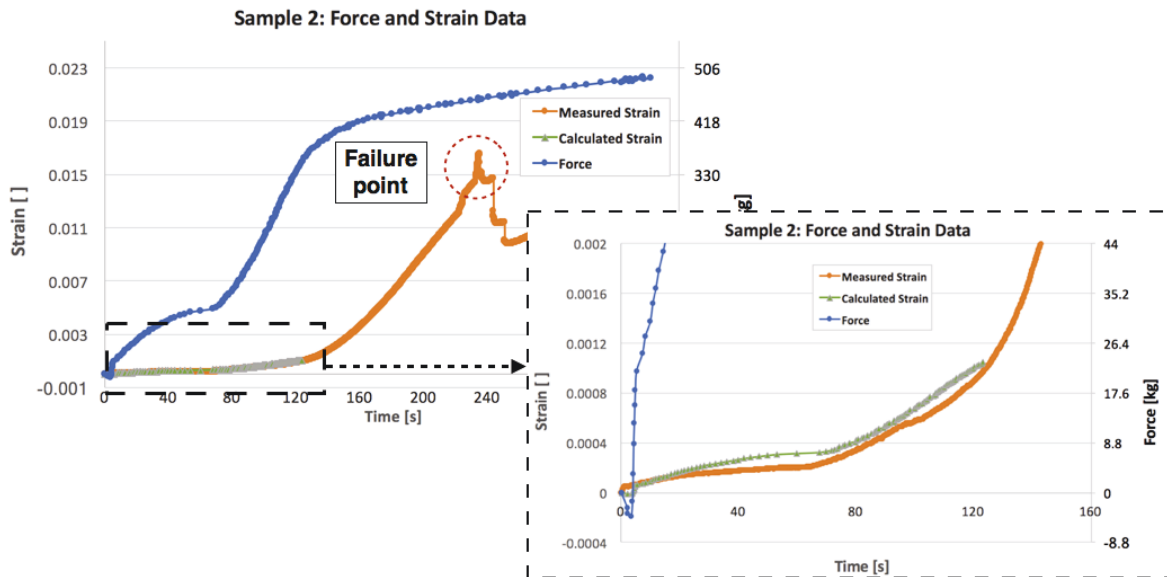
Figure 4.18: Sample 2 loaded until strain gauge failure. Strain in elastic region is also calculated from force for comparison

4.7.4 Outliers
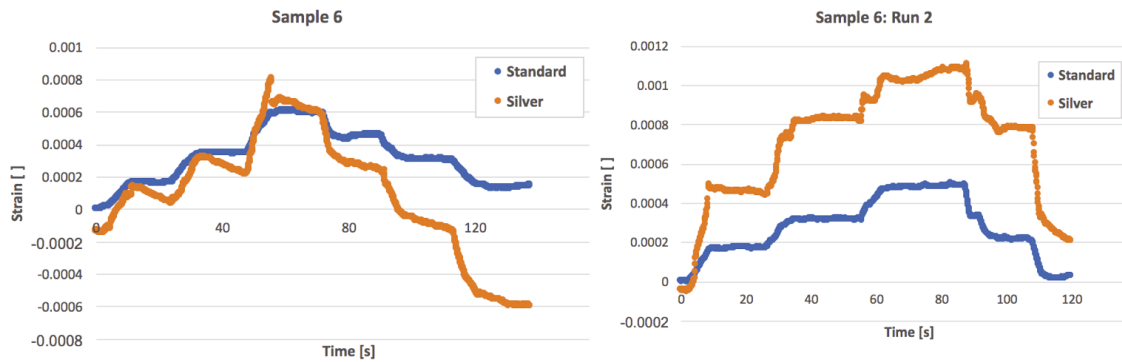
Figure 4.19: Sample 6 run twice and being compared to a standard strain gauge mounted on the other side of the tensile coupon
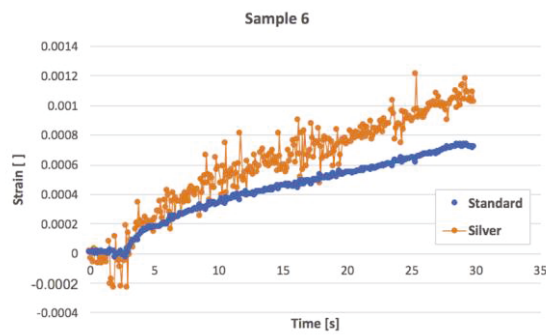

Figure 4.20: Tensile tester testing of sample 6 being compared to a standard strain gauge mounted on the other side of the tensile coupon
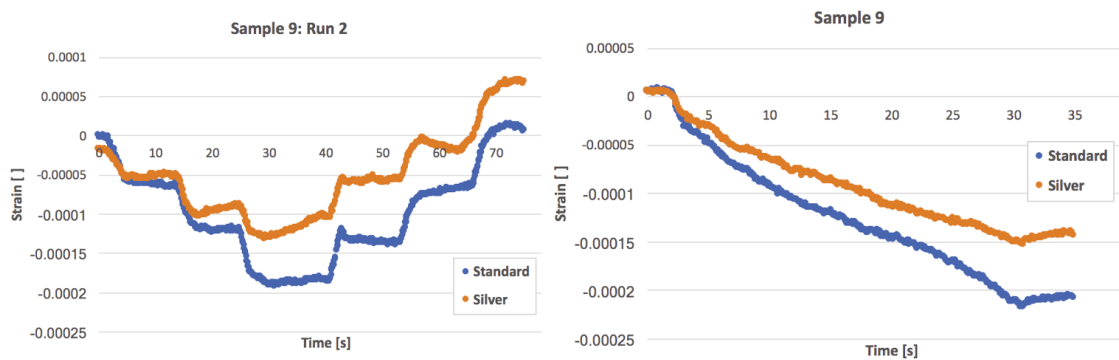
Figure 4.21: Sample 9's second run on the manual tensile tester (right) and run on the programmable tensile tester (left). Both being compared to a standard strain gauge mounted on the other side of the tensile coupon

More than ten samples were printed on kapton; unfortunately, only nine of the printed samples were functional enough to use for experimentation. The other samples either fell outside the strain gauge DAQ resistance range or gave completely unexplainable strain readings. Some of the erratic results from the ten useable samples are shown at the beginning of Section 4.7.4.

One issue that was detected during the experiments was the ohmic heating of the printed strain gauges. The NI-9237 DAQ being used for this thesis supplies a minimum current of 20mA (2.5V to a 120ohm strain gauge) to the strain gauge. This current is apparently high enough to heat up some the printed silver strain gauges. In Figure 4.19 the graph on the left shows that the strain reading kept dropping at each step and, towards the end of the experiment, it had dropped by a 100% of the maximum positive value. Although, the TCR of a strain gauge causes the resistivity (and in turn, the measured strain) to increase, the thermal expansion of a strain gauge, which causes the cross-sectional area of the grid to increase, does result in a reduction in resistance and, as such, a reduction in measured strain. What probably happened in the image on the left was that, the high current was heating up the printed strain gauge and the effects of thermal expansion outweighed the effects of the TCR; thereby causing a reduction in strain reading.

The right image on Figure 4.19 shows the second run of the same test on the same sample. The second test was carried out within two minutes of the first test and the strain was zeroed before the test began. It is possible, that after the first run, the printed strain gauge was still heated up before the second run began. Hence, the starting resistance was lower than it should have been and during the second run, the strain gauge was cooling down; thus, restoring it to its original resistance value, which resulted in the jumps in the strain reading.

Ohmic heating or its effects were not as apparent in other printed strain gauges, which points at the need to optimize the printed strain gauges by optimizing the process. Doing so, will ensure that the properties and behaviour of all printed strain gauges are known. Changing the equipment is also a viable option for dealing with ohmic heating, but optimizing the process to print more reliable strain gauges is the better option.

Figure 4.20 shows the testing of sample 6 using the programmable tensile tester. It can be seen from this figure that there is a lot more noise generated in this test than in other tests. A hypothesis regarding the source of the noise is electromagnetic interference but there is no detailed explanation as to what could be causing this.

The left image of Figure 4.21 shows sample 9 gradually deviating from the standard strain gauge readings. This result was interesting because Figure 4.15 shows that the initial run of sample 9 matched the standard strain reading. This means that there was most likely a gradual and plastic change in the microstructure of sample 9 that caused the strain gauge resistance to increase permanently. The right image of Figure 4.21 shows that the printed strain gauge no longer matches the strain readings of the standard strain gauge and this is most likely due to a change in gauge factor.

4.7.5 Thermal Response

A conventional strain gauge was subjected to the thermal testing procedure described in Section 4.6. With the conventional strain gauge being less sensitive to temperature than the printed strain gauges, the test could be carried out up to a temperature of 200°C.
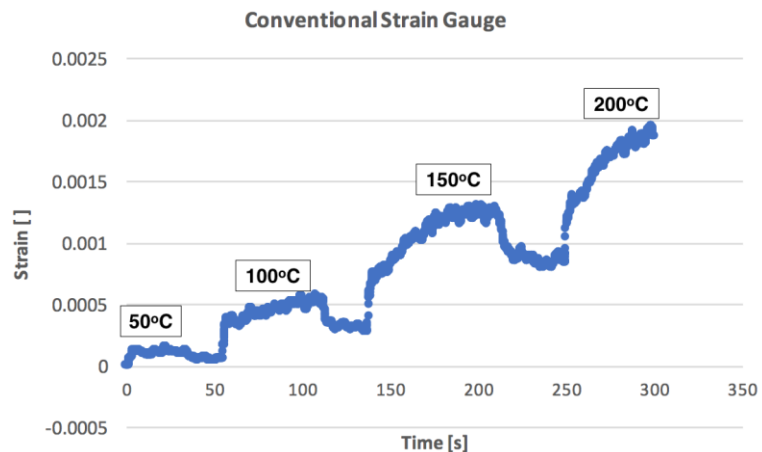
Figure 4.22: Thermal Response of Conventional Strain Gauge
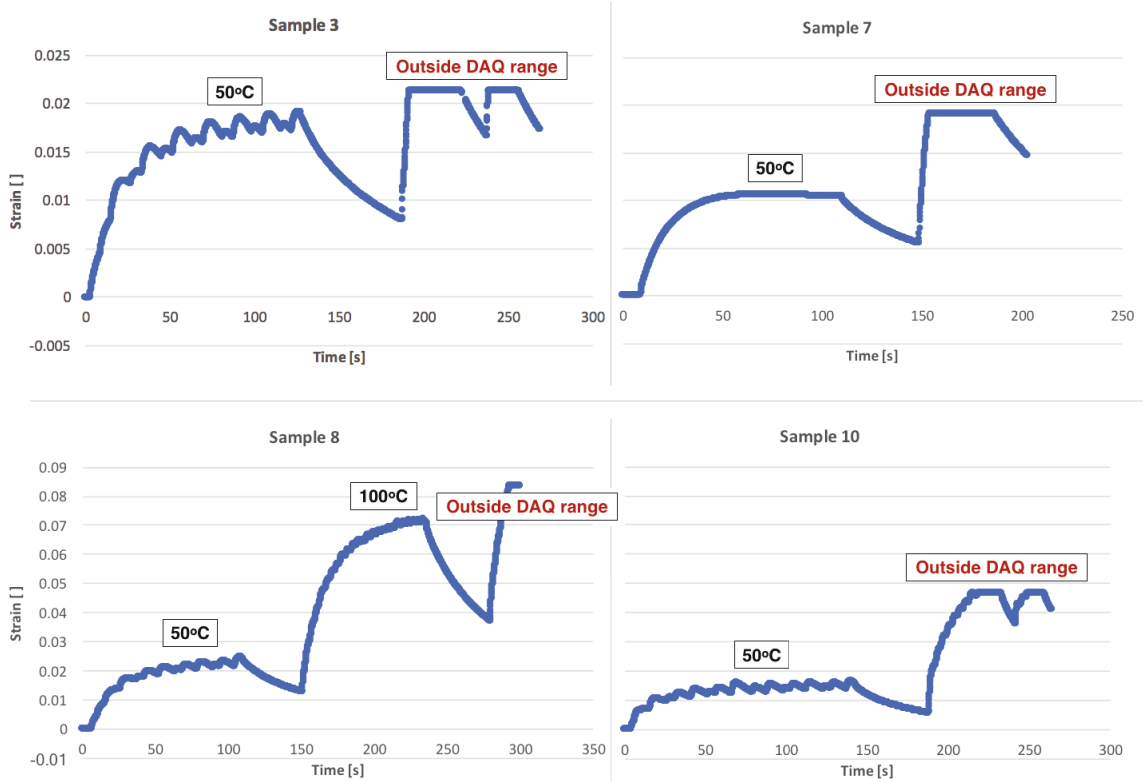
Figure 4.23: Thermal Response of Printed Samples

The thermal experiments for the printed samples had to be stopped at lower temperatures because the printed samples were significantly more sensitive to temperature and started exceeding the operating resistance range of the DAQ.

Figure 4.22 shows that conventional strain gauges are sensitive to temperature and not simply because of thermal expansion. Thermal expansion will cause a geometric change in the strain gauge that should result in a negative change in resistance, as derived in Appendix A; however, this is not the case. The derivation shows that when the strain gauge grid is exposed to temperature, in addition to the geometric induced change in resistance, there is a change in resistivity that causes an additional change in resistance. This change in resistivity is driven by the TCR of the strain gauge material and the effects can be seen in Figure 4.22 and Figure 4.23. The positive increase in resistivity dominates the total change in resistance

in such a way that, despite the drop in resistance from geometric deformation (from thermal expansion), the change in resistivity still causes the overall change in resistance to be positive.

For this thesis, the TCR was treated like a multiplier for the resistance after the effects of thermal expansion had been accounted for as per Appendix A:

$$GF = \frac{\Delta R}{R\varepsilon} \qquad \to \varepsilon = \frac{\Delta R}{R(GF)} \qquad \to \Delta R = \varepsilon(GF)R$$

$$\to from \text{ Appendix A}; \ \Delta R = -\alpha\Delta TR + \frac{d\rho}{\rho}R = -\alpha\Delta TR + (TCR)R \qquad (4.2)$$

$$\to TCR = \varepsilon(GF) + \alpha\Delta T \qquad (4.3$$

$\to$ where **GF** is 2.05 and $\boldsymbol{\alpha}$ for constantan and silver are 14.9e^{-6}K^{-1} [38] and 19.7e^{-6}K^{-1} [43], respectively

Table 4.3: Calculated TCR values based on results from Figure 4.22

Temp [ºC]	Strain Reading, ε	$\Delta\varepsilon/\Delta T$	TCR	$\Delta TCR/\Delta T$
22	0	4.29E-06	0	2.59E-05
50	0.00012	5.38E-06	6.48E-04	3.21E-05
100	0.00054	5.94E-06	2.25E-03	4.61E-05
150	0.0013	3.93E-06	4.56E-03	4.36E-05
200	0.002	9.09E-05	6.74E-03	N/A

The average differential of the strain and TCR with respect to temperature ($\frac{\Delta\varepsilon}{\Delta T}$ and $\frac{\Delta TCR}{\Delta T}$, respectively) in Table 4.3 is simply calculated by using the next temperature and strain reading, i.e. $\frac{\Delta TCR}{\Delta T}$ for 22ºC is calculated using the TCR at 50ºC. The purpose of having the TCR values or average $\frac{\Delta TCR}{\Delta T}$ is to have material property value that is associated with the temperature-induced change in resistivity and can be applied to the numerical models to make the predictions more realistic.

For the printed samples, the calculated $\frac{\Delta\varepsilon}{\Delta T}$ (based on Figure 4.23) is around **3e-4 1/ºC** for all four samples at 22ºC. For Sample 8, $\frac{\Delta\varepsilon}{\Delta T}$ at 50ºC can be calculated as **1.14e-3 1/ºC**. Comparing these values to the conventional strain gauge values in Table 4.3, it can be said that the printed silver strain gauges are a lot more sensitive (> 50 times) to temperature. This serves as an indication for the need of proper temperature compensation when working with the printed silver strain gauges at elevated temperatures.

4.8 Chapter 4 Summary

Chapter 4 started by describing the procedure of printing a functional strain gauge from silver ink. This was followed by the challenges of printing useable strain gauges. With the printed strain gauges varying in resistance, an attempt was made to rectify this by using a camera to observe the material deposition and relate that to the attained strain gauge resistance. The results of this attempt, though inconclusive at the time, show potential for a camera based printing optimization.

One of the acceptable samples printed on kapton was characterized using a laser scanning confocal microscope.

The sample preparation procedure, testing equipment used and testing procedure were described. The tensile test results for the samples printed on kapton were presented. Following each set of results, a detailed discussion, based on the observations from the results, was presented. The discussion covers some possible errors in the early stages of the experiment as well as some of the promising results from the printed strain gauges. Furthermore, it covers the results that behaved differently from what was expected and gives possible explanations as to why certain behaviors were observed. Lastly, this chapter presents the results from the thermal testing of strain gauges on kapton, discusses the thermal results and uses the results to derive a TCR property value that can be used in future COMSOL models that involve temperature.

CHAPTER 5

5 MODELLING OF TEMPERATURE-COMPENSATED STRAIN GAUGE

The aim of modelling the temperature compensated strain gauge design was to see if there were any unforeseen factors that rendered the conceptual design unfeasible. Based on the results of Sections 3 and 4, it can be said that strain gauges will primarily sense strain that is aligned with its primary axis, whether the strain gauge is mounted axially or transversely.

5.1 Description of Temperature Compensated Design

This new temperature compensated design improves on the dummy gauge temperature compensation technique described in Section 2.3.3. This design is intended for a uniaxial stress field and comprises of two strain gauges; a primary strain gauge that is aligned with the primary strain field and a dummy strain gauge that is insensitive to mechanically-induced strain. Moreover, both strain gauges will be equally sensitive to temperature and the dummy strain gauge can be used to compensate for the temperature effects on the primary strain gauge; thereby, leaving only the effects of mechanically-induced strain.

The dummy strain gauge is made insensitive to mechanically-induced strain by having the negative strain from the poisson's ratio shrinkage cancel out the primary strain. As such, the dummy strain gauge has grids aligned in the primary axis and grids aligned perpendicular to the primary axis as shown in Figure 5.1. Since the strain from the poisson's ratio shrinkage is only a fraction of the primary strain, the combined length of the grids aligned with the

shrinkage strain is longer than the combined length of the grids aligned with the primary strain. The grid lengths are a function of the poisson's ratio of the part the strain gauge is mounted to and is calculated in such a way that ensures the unloaded resistance of the dummy strain gauge matches that of primary strain gauge, while resulting in a mechanical strain of zero when exposed to a load. The resistance of both the primary and dummy strain gauge are aimed at being the same so as to achieve an equivalent temperature-induced change in resistance for the compensation.
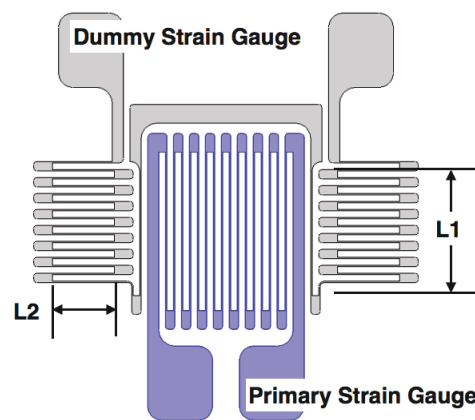
Figure 5.1: Temperature Compensated Strain Gauge Design

5.2 Governing Equation and Design

The mechanical strain insensitivity of the dummy strain gauge is achieved by letting the strain gauge experience a positive strain from the primary axis as well as a negative strain from the poisson's ratio shrinkage, which is meant to cancel out the positive strain. Since the strain is proportional to the attained total change in resistance, the design is developed using the equations for the geometric change in resistance developed in Section 3.2.5.

From Figure 5.1, L_1 represents the length of the dummy strain gauge grids aligned with the primary strain axis (axial grids), while L_2 represents the length of the dummy strain gauge

grids aligned with poisson's ratio shrinkage strain (transverse grids). L_{total} represents the total combined lengths of the grids in the primary strain gauge. In order for both the primary and dummy strain gauges to have the same unloaded resistance, they both need to have an equivalent total grid length because the grid determines a strain gauge's resistance. Therefore;

$$\rightarrow 2L_1 + 32L_2 = L_{total} \tag{5.1}$$

Regarding the change in resistance of the dummy strain gauge; let ΔR_1 represent the change in resistance of the axial grids and let ΔR_2 represent the change in resistance of the transverse grids. Also, let ε_1 represent the strain in the primary strain axis and ε_2 represents the strain perpendicular to the primary axis, which is equal to the shrinkage strain (i.e. $\varepsilon_2 = -v\varepsilon_1$; where v is the poisson's ratio of the part the strain gauge is mounted to).

Recall, $GF = \dfrac{\Delta R}{R\varepsilon}$ $\qquad \rightarrow \Delta R = R.GF.\varepsilon$

Recall, $R = \rho\dfrac{L}{A}$ $\qquad \rightarrow \Delta R = \rho\dfrac{L}{A}.GF.\varepsilon$ $\qquad \rightarrow \dfrac{\Delta R_1}{\Delta R_2} = \dfrac{\rho\dfrac{2L_1}{A}.GF.\varepsilon_1}{\rho\dfrac{32L_2}{A}.GF.\varepsilon_2}$

Considering that both the axial and transverse grids will be printed around the same time, it can be assumed that both grids will have the same resistivity, ρ, gauge factor, GF, and cross-sectional area, A. Therefore;

$$\rightarrow \frac{\Delta R_1}{\Delta R_2} = \frac{2L_1.\varepsilon_1}{32L_2.\varepsilon_2} \tag{5.2}$$

Since the dummy strain gauge is meant to be insensitive to mechanically-induced strain, the combined change in resistance should result in a value of 0. Therefore;

$\rightarrow \Delta R_1 + \Delta R_2 = 0$ $\qquad \rightarrow \dfrac{\Delta R_1}{\Delta R_2} = -1$ $\qquad \rightarrow \dfrac{\Delta R_1}{\Delta R_2} = \dfrac{2L_1.\varepsilon_1}{32L_2.\varepsilon_2} = -1$

Recall, $\varepsilon_2 = -v\varepsilon_1$ $\qquad \rightarrow \dfrac{\varepsilon_1}{\varepsilon_2} = \dfrac{\varepsilon_1}{-v\varepsilon_1} = -\dfrac{1}{v}$

$$\rightarrow \frac{2L_1.\varepsilon_1}{32L_2.\varepsilon_2} = -1 = -\frac{2L_1}{32L_2.v}$$

$$\rightarrow L_1 = 16L_2.v \qquad\qquad\qquad\qquad\qquad\qquad\qquad\qquad (5.3)$$

L_{total} from the primary strain gauge = 16(1.59) = 25.44mm

Hence, by solving equation 1 and 2 with $v = 0.285$: $\boldsymbol{L_1 = 2.88mm}$ and $\boldsymbol{L_2 = 0.62mm}$

All other supplementary geometries and dimensions such as the grid width, strain gauge thickness, end loops and solder pads, match those of the primary strain gauge as per Appendix B.

With L_1 being longer than anticipated, some minor design modifications needed to be made; thus, resulting in the final design shown in Figure 5.2.
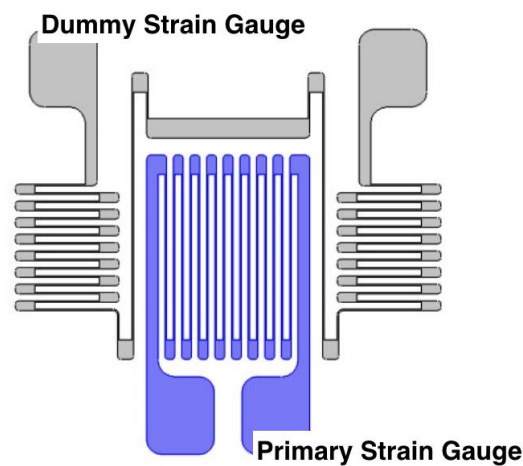
Figure 5.2: Final Temperature Compensated Design

5.3 COMSOL Model

The COMSOL model for the temperature compensated design is made very much like the models described in Section 3.2. The materials used and meshing technique do not change in comparison to Section 3.2, but there are differences in the strain gauge design and boundary conditions.

5.3.1 Assembly and Material Properties

Unlike the model described in Section 3.2, this model has two strain gauges as opposed to one. The sketch of the dummy strain gauge is created in AutoCAD and exported into Solidworks to be extruded to a thickness 7μm. Another difference is that, this model does not have the kapton encapsulation layer. A study was done on the effect of the encapsulation layer and the study showed that the encapsulation layer has no effect on the strain gauge performance. As such, the encapsulation layer was removed to reduce the total number of mesh elements in the model; thereby, reducing computation time.

The thermal properties for each material in the simulation is tabulated in Table 5.1.

Table 5.1: Material Thermal Properties

Property	Material		
	Steel 1018 [36]	**Polyimide** [37]	**Constantan** [38]
Thermal Expansion	12.3e-6 1/K	50e-6 1/K	14.9e-6 1/K
Specific Heat Capacity	475 J/(kg.K)	1100 J/(kg.K)	390 J/(kg.K)
Thermal Conductivity	44.5 W/(m.K)	0.12 W/(m.K)	19.5 W/(m.K)

5.3.2 Boundary Conditions

As this model was aimed at investigating the effects of temperature, some thermal boundary conditions had to be added to the model. A temperature boundary condition was put on the front surface of the strain gauges, the uncovered surface of the kapton substrate and a portion

of the uncovered tensile coupon close to the strain gauges. The locations of the mechanical boundary conditions were kept the same as in Section 3.2.
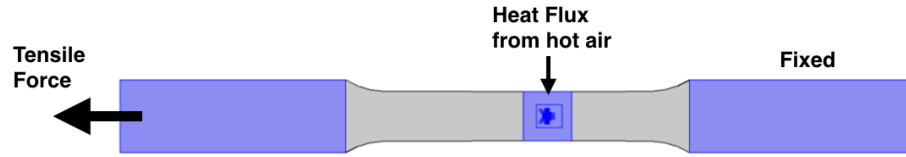
Figure 5.3: Thermal and mechanical boundary conditions for temperature compensated strain gauge model

The loading history for this model was a combination of mechanical strain and temperature, with the aim being to see whether the new design would compensate for the effects of temperature. The target loading strains and temperatures are shown below in Table 5.2.

Table 5.2: Target strain and temperatures for temperature compensated model

Strain	0	0.0003	0.0006	0.0009	0.002
Temperature [K]	293	323	373	423	

All combinations of strain and temperature were run to result in a total of 20 combinations.

5.3.3 Meshing

Table 5.3: (Right) Number of grid mesh elements
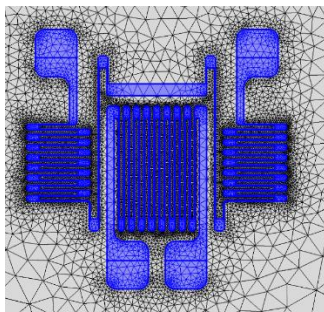
Strain Gauge	Grid Orientation	# of Elements
Primary	Axial	55
Dummy	Axial	85
Dummy	Transverse	35

Figure 5.4: (Left) Meshing of temperature compensated model

This model was meshed with triangular mesh elements swept from the front surfaces of the strain gauges to the back surfaces of the tensile coupon as shown in Figure 5.4. The grids of the primary and dummy strain gauges are given fixed numbers of mesh elements for resistance extraction accuracy. The assigned number of grid elements is shown in Table 5.3.

5.4 Results and Discussion

5.4.1 Strain Field and Change in Resistance

As expected, the strain in the grids is significant when the grids are aligned with the strain field and negligible when the grids are aligned perpendicular to the strain field as per Figure 5.5. The primary grids from both the primary and dummy strain gauges experience a positive strain while the transverse grids from the dummy strain gauge experience a negative strain that is meant to cancel out the effects of the positive strain on the primary grids.

Figure 5.5: Strain Field in the X and Y direction from the Temperature Compensated Model at Room Temperature (left) and at 423K (right)

74

Figure 5.5 shows that the grids receive the right amount of strain depending on the grid orientation i.e. grids aligned in the y orientation will experience the same amount of y-strain experienced by the part u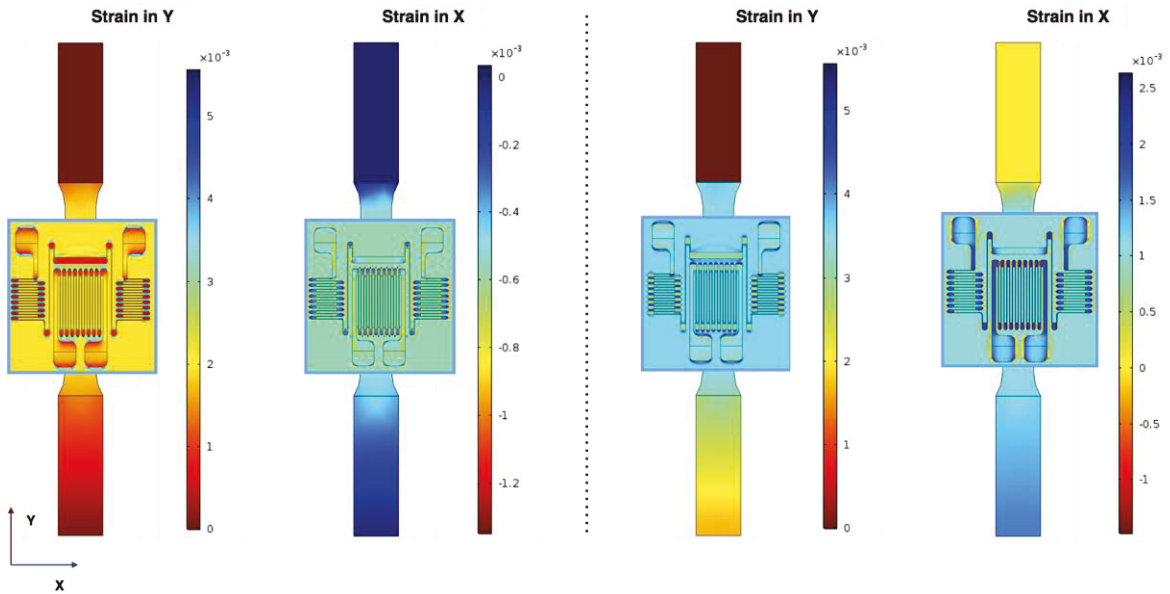nderneath, but not the same amount of x-strain. In a similar fashion, grids aligned in the x orientation will experience the same amount of x-strain as the part underneath, but not the same amount of y-strain. This allows the dummy strain gauge to work as expected since it will experience the right amount of positive y strain and the right amount of negative x strain to result in a total mechanical strain of zero. Figure 5.5 also shows how the effects of thermal expansion adds a positive strain in all directions; thus, making the strain in the transverse grids of the dummy gauge positive. Since this thermal strain is experienced everywhere, the transverse grids of the dummy strain gauge now being positive is only part of the compensation mechanism and does not hinder the overall performance of the design.

In addition, it is important to note that, with such small mechanical strains applied, the effects of thermal expansion on the steel coupon are significant enough to cause a shift in the strain field. For example, the y-strain goes from 0.002 to ~0.00325 when the temperature is changed from 293K to 423K. However, the compensated design still gives a resultant strain reading of 0.002 at 423K (Figure 5.6). This means that temperature compensation design eliminates all effects of temperature, even the thermal expansion of the part underneath the strain gauge. Whether, this is beneficial or detrimental depends on the application.

The deformed mesh from the structural simulation is exported into an electrical simulation and the change in resistance is obtained. The obtained change in resistance is driven by both, the thermal expansion of the strain gauge and the applied mechanical force. As such, the obtained change in resistance from increasing the temperature is negative at this stage; as is expected from the derivation in Appendix A. The results as received from COMSOL are shown in Figure 5.6. For the "Without compensation" graph on the left, only the results of the primary strain gauge is shown. However, for the compensation, the strain from the dummy strain gauge is subtracted from the strain from the primary strain gauge to produce the temperature compensated strain.
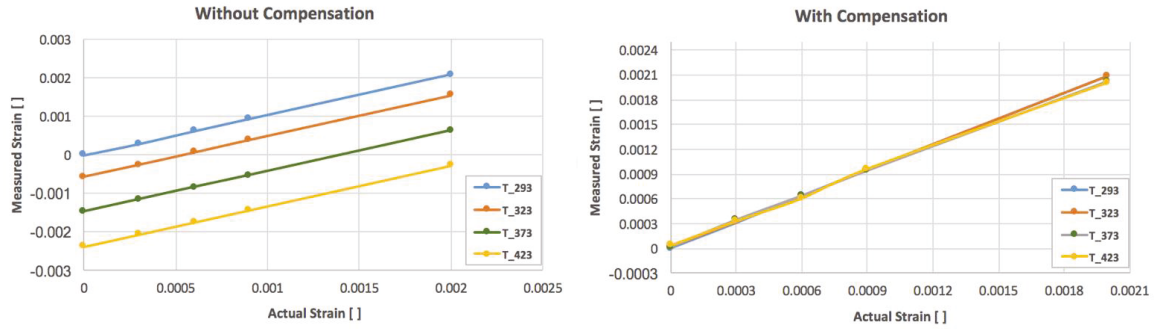
Figure 5.6: Measured strain from modelled strain gauge at different temperatures without compensation design (left) and with compensation design (right)

Figure 5.6 shows the modelled effects of higher temperatures on strain gauge strain readings. On the plot without compensation, the measured strain is dropping with increased temperature. This means that in the model the resistance is dropping with increased temperature. This is accurate when only the effects of thermal expansion are considered without considering the effects of the material's TCR. Incorporating the TCR into the COMSOL results merely raises and magnifies result. Moreover, if the TCR was being incorporated, it would have been applied to both the primary and dummy strain gauge readings and the result would have ended up being very similar to the right plot of Figure 5.6, which shows that the results at higher temperatures after compensation match the result at room temperature.

5.4.2 Incorporating TCR Effect into the Model

In order to make the results realistic, the TCR values derived in Section 4.7.5 are incorporated into the COMSOL result by introducing a temperature coefficient of resistivity correction factor, C_{TCR}. The new resistance after thermal loading is multiplied by the correction factor to account for the TCR effect, which causes a temperature-induced change in resistivity. C_{TCR} is derived as follows:

$$\rightarrow R_2 = R + \Delta R = C_{TCR}R'_2 = C_{TCR}(R - \alpha \Delta T R)$$

76

where R'_2 represents the new resistance from COMSOL which only accounts for the geometric effects from thermal expansion

$\rightarrow Recall\ (Section\ 4.7.5), \Delta R = -\alpha \Delta T R + (TCR)R$

$\rightarrow Therefore;\ R_2 = R - \alpha \Delta T R + (TCR)R = C_{TCR}(R - \alpha \Delta T R)$

$\rightarrow C_{TCR} = 1 + \dfrac{TCR}{1 - \alpha \Delta T} \approx 1 + TCR$

The results of incorporating C_{TCR} into the COMSOL results were compared to the experimental values for a conventional strain gauge obtained from Figure 4.22. The comparison between the experimental results and the TCR adjusted model results without mechanical load and compensation is shown in Figure 5.7. Added to the same plot, is the TCR adjusted modelled result after compensation.
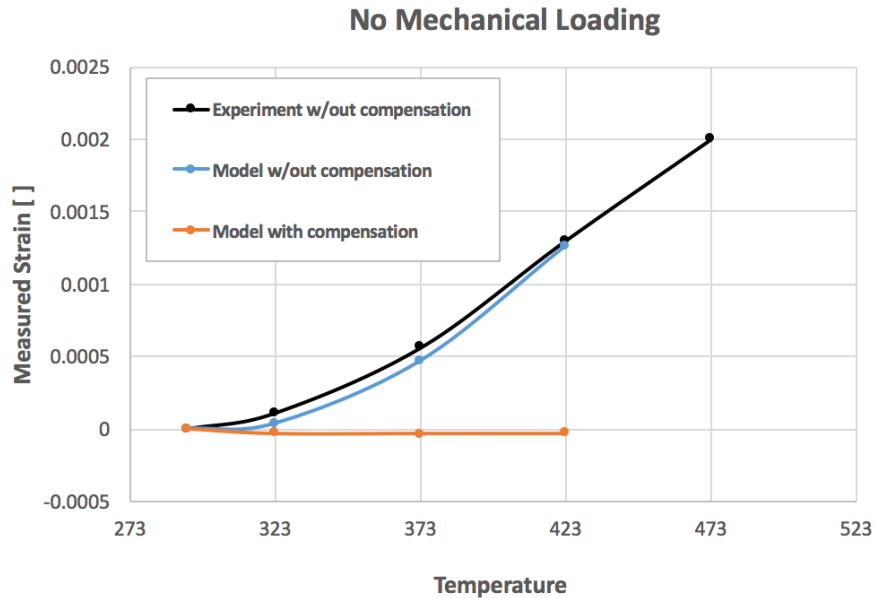

Figure 5.7: Experimental Results and Modelled Results with TCR incorporated but, without Mechanical Load

The C_{TCR} correction was not incorporated into the results with mechanical load applied because doing so would require the piezoresistive correction factor, C_{pz}, derived in Section

77

3.4.4, to be incorporated into the adjustment as well. To do so, the geometrically-induced resistance change from temperature and mechanical loading need to be separated and adjusted differently. While it is possible to achieve this, it was not done because the aim of this model was to observe the behaviours of the primary and dummy strain gauges and note whether the dummy strain gauge provided the necessary compensation. Since Figure 5.6 answers this question and incorporating the TCR and piezoresistive effects basically magnifies and shifts these results there was no need to get the results with the incorporated piezoresistive correction.

Lastly, Figure 5.7 is meant to serve as a means of validating the model and the developed correction factor. This is a preliminary simulation because only one conventional strain gauge was used to derive the TCR values. Although several conventional strain gauges were subjected to the thermal experiment (as shown in Appendix C), the result of that experiment was inconclusive. Therefore, it is unsure as to whether the derived TCR values are accurate. However, the results in Figure 5.7 show that the procedure can be used for predicting the behavior of strain gauges at higher temperatures when the appropriate TCR values are known.

5.5 Chapter 5 Summary

Chapter 5 described the governing theory behind the temperature compensated design. This was then followed by deriving the governing equation for the geometric features of the design.

The temperature compensated design COMSOL model was described and the changes from the COMSOL models in Section 3.2were highlighted. Two main results were shown for the temperature compensated model. The first being the strain field on the grids and the second being model-predicted strain that is derived from the change in strain gauge resistance. Work involving incorporating the derived TCR values from Section 4.7.5 into the COMSOL model results without considering mechanical loading was also done and the result of this was also presented.

The promising results of the modeled temperature compensation design was discussed. It was stated that, the temperature compensation design also eliminates the effects of the substrate's (or part's) thermal expansion. The results with the TCR incorporated matched the experimental result with no mechanical load applied and a reason was given as to why the TCR was not used on results with applied mechanical load.

Lastly, it was stated that the preliminary study of incorporating the TCR into the COMSOL results helps validate the result but the attained TCR values are questionable since they were only derived from one conventional strain gauge sample.

CHAPTER 6

6 CONCLUSIONS AND FUTURE WORK

6.1 Conclusions

From this thesis, the following conclusions can be drawn;

1. By being able to directly print strain gauges on a part, aerosol jet printing provides an opportunity to reduce the time, labor and placement errors that come with manually mounting multiple strain gauges on a part during strain field mapping. With aerosol jet printing being a CAD based printing process that prints selective patterns based on a specified/customized vector path, a CAD file with several strain gauges in specified locations can be created. The part of interest can be fixed in place within the aerosol jet printer and all the strain gauges can be printed in one pass. With the accuracy of the printer there is a guarantee that the placement error of the printed strain gauges will be $< 1\mu$m. Customized strain gauge patterns can also be created easily by simply modifying the CAD file, and these customized patterns can be tailored to measure strain fields more precisely than conventional strain gauges. Aerosol jet printing is also capable of printing on non-planar surfaces, which means that the concept of printing strain gauges directly on parts can be applied to a wider range of parts and not only flat surfaces.

2. The gauge factor of a strain gauge, a property that maps the change in resistance to the applied strain, can be broken down into the geometric and piezoresistive components. The geometric component is driven by the deformation of the strain

gauge and is dependent on the poisson's ratio of the strain gauge material. The piezoresistive component is driven by a strain-induced change in resistivity that is caused by the deformation of the lattice structure of the strain gauge material. The geometric component can easily be determined because the poisson's ratio of a material is a readily available property. However, the piezoresistive property is not a readily available and needs to be determined via experimentation.

3. Strain gauges are primarily meant to sense strain acting in the primary axis of the strain gauge. Strain acting parallel to the primary axis of the strain gauge will cause a significant change in resistance, which is dependent on the gauge factor of the strain gauge. When strain acts perpendicular to the primary axis (transverse strain) of the strain gauge, there are a few factors that will influence whether it will cause a significant change in resistance or not. The amount of surface area for the transfer and the stiffness of the materials involved are the major factors. If the stiffness of the substrate is less than that of the strain gauge, then the substrate will be incapable of completely transferring the transverse strain to the strain gauge. Hence, in the case of a conventional strain gauge, which comprises of a constantan strain gauge on a polyimide substrate, transverse strain barely gets transferred to the strain gauge and errors from transverse sensitivity are negligible. However, when the stiffness of the substrate is greater than the stiffness of strain gauge (as is the case with printing directly on a coated part), all the strain in the substrate will be transferred to the strain gauge. This includes transverse strain, which could introduce errors in the measured strain.

4. The numerical model and the derived piezoresistive correction factor are valid since the predicted transverse sensitivity from the model matched the transverse sensitivity stated by the strain gauge manufacturer.

5. Successful printing and sintering of a silver strain gauge results in a strain gauge with a resistance in the 110 - 130Ω range. The printed strain gauge has a smooth surface and the grids take the approximate form of rectangular prisms with a width of 60μm and a height or thickness of 15μm.

6. There are uncertainties in the strain gauge printing process that cause variabilities in the printed sensors, and these variabilities make the performance of the printed sensors unpredictable. One potential solution for eliminating these variabilities is using a camera to monitor the print deposition area of a line before printing a strain gauge. This optimization process still requires work and validation, but shows potential for achieving uniform printed strain gauge properties.

7. When an ideal strain gauge is printed, it behaves similar a conventional strain gauge and has a linear response to applied strain. The gauge factors of the printed strain gauges varied from sensor to sensor due to uncertainties in the printing process; however, the gauge factor for a particular sensor remained constant during loading. Some of the printed sensors produced erratic and unexpected results but this can be blamed on the printing process leading to different microstructures after sintering. One of the printed strain gauges was loaded until failure and failed at a strain of 1.6%. Although this is only half the failure strain of a conventional strain gauge, it is a promising result, considering the fact that the printed strain gauges are made up of sintered nanoparticles. From the thermal experiments, it can be concluded that the printed silver strain gauges are highly more sensitive to temperature than conventional constantan strain gauges (> 50 times).

8. Based on the model, the temperature compensated strain gauge design works as expected. In a combined mechanical and thermal loading scenario, the temperature

82

compensated design completely eliminates all effects of temperature (even the thermal expansion of the part) to result in a strain reading that represents only the mechanically-induced strain on the part.

6.2 Future Work

There are several areas of this thesis that require more work and improvement.

The printing of silver strain gauges can sometimes result in acceptable strain gauges, but being unable to predict the performance of the printed strain gauge until the strain gauge is sintered and tested, is a problem that greatly reduces the efficiency of the process. The time and material wasted on printing and sintering unreliable sensors needs to be eliminated in order to make this process an ideal sensing alternative. In situ monitoring of either the material deposition or the ink concentration can help in ensuring that every printed sensor has a uniform set of properties and produces an acceptable performance.

Upon optimizing the printing process, the testing process can be modified to attain more conclusive results about the failure strain and thermal response of the printed strain gauges. It is assumed that upon optimizing the printing process, the gauge factor of the printed strain gauges will be a fixed number that stays the same for all sensors printed with the same material deposition and sintering process. With that variability eliminated, a more in depth characterisation of the printed sensors can be done. The more in-depth characterization can include a CT scan, which will help determine the amount of porosity in the printed strain gauges.

A more in-depth understanding of printing and sintering parameters and how they affect the properties of the printed sensors can also be done. This will require that either material deposition or ink concentration be kept constant while other parameters be changed. The resultant printed strain gauges can then be subjected to analysis to understand which parameters led to a higher resistance, gauge factor or porosity.

Lastly, additional validation of some of the modeled results is required. Strain gauges need to be printed on coated tensile coupons and tested. Printing on coated tensile coupons will help validate the predicted strain gauge performance for when the substrate is stiffer than the strain gauge. The temperature compensation design also needs to be printed on a kapton substrate, mounted to a tensile coupon, and subjected to both mechanical and thermal loading to determine if the compensation is as good as the model predicts.

REFERENCES

[1] J. Fields, G. Pach, K. Horowitz, T. Stockert, M. Woodhouse and M. v. Hest, "Printed interconnects for photovoltaic modules," *Solar Energy Material &Solar Cells,* vol. 159, pp. 536-545, 2017.

[2] R. S. Aga, J. P. Lombardi, C. M. Bartsch and E. M. Heckman, "Performance of a Printed Photodetector on a Paper Substrate," *IEEE Photonics Technology Letters,* vol. 26, no. 3, pp. 305-308, 1 February 2014.

[3] N. Bolse, R. Eckstein, M. Schend, A. Habermehl, G. Hernandez-Soza, C. Eschenbaum and U. Lemmer, "Discrimination of trace nitroaromatics using linear discriminant analysis on aerosol jet printed fluorescent sensor arrays," in *SPIE,* 2017.

[4] T. Rahman, A. Rahimi, S. Gupta and R. Panat, "Microscale additive manufacturing and modeling of interdigitated capacitive touch sensors," *Sensors and Actuators A: Physical,* vol. 248, pp. 98-103, 14 July 2016.

[5] J. Puy-Llovera, C. Perez-Rafols, N. Serrano, J. M. Diaz-Cruz, C. Arino and M. Esteban, "Selenocystine modified screen-printed electrode as an alternative sensor for the voltammetric determination of metal ions," *Talanta ,* vol. 175, pp. 501-506, 2017.

[6] S. Li, J. G. Park, S. Wang, R. Liang, C. Zhang and B. Wang, "Working mechanisms of strain sensors utilizing aligned carbon nanotube network and aerosol jet printed electrodes," *Carbon,* vol. 73, pp. 303-309, 2014.

[7] A. Blayo and B. Pineaux, "Printing Processes and their Potential for RFID Printing," in *Joint sOc-EUSAI conference ,* Grenoble, 2005.

[8] M. Smith, Y. S. Choi, C. Boughey and S. Kar-Narayan, "electronics, Controlling and assessing the quality of aerosol jet printed features for large area and flexible," *Flexible and Printed Electronics,* vol. 2, pp. 1-11, February 2017.

[9] H. R. Bankhead and C. E. Meece, "Stress mapping of a low pressure compressor for an advanced turbojet engine," in *The American Society of Mechanical Engineers*, New York, 1984.

[10] K. Andrew, "Sine Test Preparation & Management Involving Large Number Of Channel Counts," in *4th ECCOMAS Thematic Conference on Computational Methods in Structural Dynamics and Earthquake Engineering*, Kos Island, 2013.

[11] D. D. Sargent, R. M. E., B. Bakht and A. A. Mufti, "Structural Health Monitoring of Lindquist Bridge," in *SPIE*, 2007.

[12] R. A. Clark, A. Franklyn-Miller, E. Falvey, A. L. B. S. Bryant and P. McCrory, "Assessment of mechanical strain in the intact plantar fascia," *The Foot,* vol. 19, pp. 161-164, 2 June 2009.

[13] S. A. Gee, W. F. Van Den Bogert and V. R. Akylas, "Strain-Gauge Mapping of Die Surface Stresses," *IEEE Transactions of components, hybrids and manufacturing technology,* vol. 12, no. 4, pp. 587-593, December 1989.

[14] R. R. Magalhaes, B. A. Vieira Junior and S. R. Barra, "The use of conventional strain gauges evaluation for measurements of residual stresses in welded joints," *J Braz. Soc. Mech. Sci. Eng.,* vol. 36, pp. 173-180, 2014.

[15] H. J. Lee, M.-G. Kim, M. Shikida and K. Sato, "A Table-Shaped Tactile Sensor for Detecting Triaxial Force on the Basis of Strain Distribution," *Sensors,* vol. 13, pp. 16347-16359, November 2013.

[16] C.-H. Pi and K.-S. Chen, "A strain-sensing based scheme for indoor localization: Analysis, algorithm, and demonstration," *Measurements,* vol. 51, pp. 224-235, 2014.

[17] Micro-mesurements, "Strain Gage Installations with M-Bond 200 Adhesive," 30 December 2014. [Online]. Available: http://www.vishaypg.com/docs/11127/11127B127.pdf. [Accessed 24 August 2017].

[18] T. H. Eom and J. I. Han, "The effect of the nickel and chromium concentration ratio on the temperature coefficient of the resistance of a Ni–Cr thin film-based temperature sensor," *Sensors and Actuators A,* vol. 260, pp. 198-205, 2017.

[19] L. J. Deiner and T. L. Reitz, "Inkjet and Aerosol Jet Printing of Electrochemical Devices for Energy Conversion and Storage," *Advanced Engineering Materials,* vol. 19, no. 7, pp. 1-18, 2017.

[20] T. Seifert, E. Sowade, F. Roscher, M. Wiemer, T. Gessner and R. R. Baumann, "Printing, Additive Manufacturing Technologies Compared: Morphology of Deposits of Silver Ink Using Inkjet and Aerosol Jet," *Industrial and Engineering Chemical Research,* vol. 54, pp. 769-779, January 2015.

[21] Y. Zhang, L. Wu, X. Guo, Y.-G. Jung and J. Zhang, "Molecular dynamics simulation of electrical resistivity in sintering process of nanoparticle silver inks," *Computational Materials Science,* vol. 125, pp. 105-109, 2016.

[22] S.-Z. Guo, K. Qiu, F. Meng, S. H. Park and McAlpine, "3D Printed Stretchable Tactile Sensors," *Advanced Materials,* vol. 29, pp. 1-8, 2017.

[23] Y. Ge, M. Plotner, A. Berndt, A. Kumar, B. Voit, D. Pospiech and W.-J. Fischer, "All-printed capacitors with continuous solution dispensing technology," *Semiconductor Science and Technology,* vol. 32, pp. 1-6, 17 August 2017.

[24] K. Takagishi, Y. Suzuki and S. Umezu, "The high precision drawing method of chocolate utilizing electrostatci ink-jet printer," *Journal of Food Engineering ,* vol. 216, pp. 138-143, 2018.

[25] E. Jabari and E. Toyserkani, "Micro-scale aerosol-jet printing of graphene interconnects," *Carbon,* vol. 91, pp. 321-329, May 2015.

[26] A. B. Marin and M. Hedges, "Optomec: 3D Aerosol Jet® Printing - Adding Electronics Functionality to RP/RM," in *DDMC 2012 Conference*, Berlin, 2012.

[27] C. Cao, J. B. Andrews and A. D. Franklin, "Completely Printed, Flexible, Stable, and Hysteresis-Free Carbon Nanotube Thin-Film Transistors via Aerosol Jet Printing," *Advanced Electronic Materials,* vol. 3, 2017.

[28] M. J. Catenacci, P. F. Flowers, C. Cao, J. B. Andrews, A. D. Franklin and B. J. Wiley, "Fully Printed Memristors from Cu–SiO2 Core–Shell Nanowire Composites," *Electronic Materials,* vol. 46, no. 7, pp. 4596-4603, 2017.

[29] Omega, "Strain Gage Technical Data," [Online]. Available: https://www.omega.ca/ techref/pdf/STRAIN_GAGE_TECHNICAL_DATA.pdf. [Accessed 27 August 2017].

[30] Omega Engineering Inc, "Strain Gages, Accessories and Instrumentation," Omega Engineering Inc, [Online]. Available: http://www.omega.ca/section_eng/strain-gages-accessories.html. [Accessed 27 August 2017].

[31] A. G. Al-Sehemia, A. A. Al-Ghamdic, N. Dishovskyd, N. T. Atanasove and G. L. Atanasovae, "Flexible and small wearable antenna for wireless body area network applications," *Journal of Electromagnetic Waves and Applications,,* vol. 31, no. 11-12, pp. 1063-1082, May 2017.

[32] R. L. Hannah and S. E. Reed, Eds., Strain Gage Users' Handbook, Springer Netherlands, 1992.

[33] National Instruments, "Products," [Online]. Available: http://www.ni.com/en-ca/shop.html. [Accessed 28 August 2017].

[34] A. Erturk and D. j. Inman, Piezoelectric Energy Harvesting, West Sussex: John Wiley and Sons Ltd, 2011.

[35] VPG-Micro-measurements, "Introduction to Strain Gage Technology," [Online]. Available:
http://www.egr.unlv.edu/~bj/MEG_302L_web/Student_strain_gage_Manual-001.PDF. [Accessed 28 August 2017].

[36] ASM Aerospace Specifications Metals Inc., "AISI 4340 Steel, normalized, 100 mm (4 in.) round," [Online]. Available: http://asm.matweb.com/search/SpecificMaterial.asp?bassnum=m434ae. [Accessed 29 August 2017].

[37] Dupont Kapton, "Summary of properties," [Online]. Available: http://www.dupont.com/content/dam/dupont/products-and-services/membranes-and-films/polyimde-films/documents/DEC-Kapton-summary-of-properties.pdf. [Accessed 29 August 2017].

[38] Roymech, "Properties of Solids," [Online]. Available: http://www.roymech.co.uk/Useful_Tables/Matter/Prop_Solids.htm. [Accessed 29 August 2017].

[39] Vishay Precision Group, "Errors due to transverse sensitivity in strain gauges," 28 June 2011. [Online]. Available: http://www.vishaypg.com/docs/11059/tn509tn5.pdf. [Accessed 10 September 2017].

[40] R. Mike, *Process Optimization,* Optomec, Inc, 2011.

[41] L. L. Hench and J. K. West, "The Sol-Gel Process," *Chemical Reviews,* vol. 90, pp. 33-72, 1990.

[42] D. R. Smith and F. R. Fickett, "Low-Temperature Properties of Silver," *Journal of Research of the National Institute of Standards and Technology,* vol. 100, no. 119, pp. 119-172, 1995.

[43] Agilent Technologies, "Laser and Optics User's Manual: Chapter 17: Material Expansion Coefficients," 2002. [Online]. Available: https://psec.uchicago.edu/thermal_coefficients/cte_metals_05517-90143.pdf. [Accessed 16 September 2017].

[44] VPG-Micro-measurements, "062AP Pattern Layout. Dwg #: 70-091516A-T," 30 October 2015. [Online]. [Accessed 28 August 2017].

[45] R. Eckstein, "Aerosol Jet Printed Electronic Devices and Systems," Karlsruher Institute of Technology, 2016.

APPENDICES

Appendix A

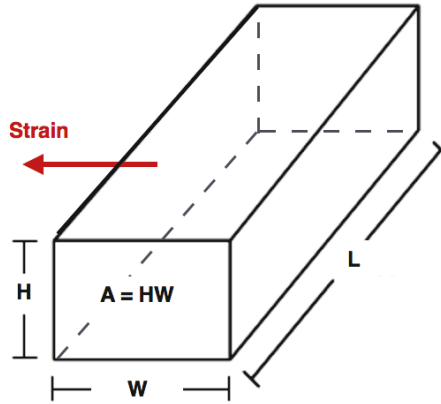**Change in Resistance Derivations**

Figure A. 1: Single Grid Approximation with Strain in the Transverse Direction

$$R = \rho \frac{l}{A}, \qquad \text{Strain from part underneath strain gauge grid} = \varepsilon_w \; or \; \varepsilon_{transverse}$$

$$\rightarrow \Delta R = \frac{\partial R}{\partial l} dl + \frac{\partial R}{\partial A} dA + \frac{\partial R}{\partial \rho} d\rho = \frac{\rho}{A} dl - \frac{\rho}{A^2} dA + \frac{l}{A} d\rho$$

$$\rightarrow \frac{\Delta R}{R} = \frac{dl}{l} - \frac{dA}{A} + \frac{d\rho}{\rho}$$

$$\rightarrow Aside: \frac{dl}{l} = -v\varepsilon_w,$$

$$\rightarrow Aside: \frac{dA}{A} = \frac{(H+dH)(W+dW)-HW}{HW} = \frac{H(\varepsilon_w W)+W(-v\varepsilon_w H)+[-v\varepsilon_w{}^2 HW \approx 0]}{HW}$$

$$\rightarrow Aside: \frac{dA}{A} \approx (1-v)\varepsilon_w$$

91

$$\rightarrow \frac{\Delta R}{R} = \frac{dl}{l} - \frac{dA}{A} + \frac{d\rho}{\rho} \approx -\varepsilon_w + \left(\frac{d\rho}{\rho}\right)_{transverse}$$

$$\rightarrow \Delta R \approx -\varepsilon_w R + \left(\frac{d\rho}{\rho}\right)_{transverse} R$$

$$\Delta R \equiv Geomtric\ Factor + Resistivity\ Factor$$

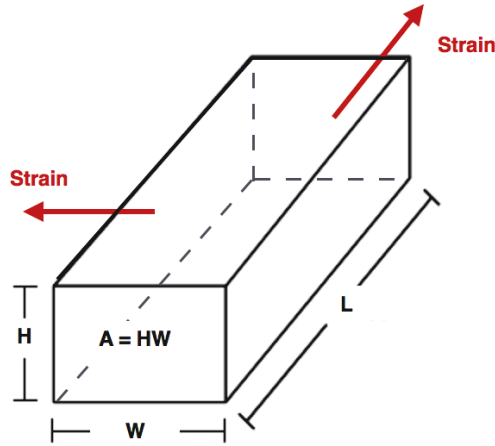$$\therefore GF_{geometric} = \frac{\Delta R}{R\varepsilon_w} = \frac{-\varepsilon_w R}{R\varepsilon_w} = -1$$

Figure A. 2: Single Grid Approximation with Strain in both Axial and Transverse Direction

$$R = \rho\frac{l}{A}, \qquad \text{Axial and transverse strain from part underneath strain gauge grid} =$$

$$\varepsilon_l\ and\ \varepsilon_w\ , \text{respectively}$$

$$\rightarrow \Delta R = \frac{\partial R}{\partial l}dl + \frac{\partial R}{\partial A}dA + \frac{\partial R}{\partial \rho}d\rho = \frac{\rho}{A}dl - \frac{\rho}{A^2}dA + \frac{l}{A}d\rho$$

$$\rightarrow \frac{\Delta R}{R} = \frac{dl}{l} - \frac{dA}{A} + \frac{d\rho}{\rho}$$

$$\rightarrow Aside: \frac{dl}{l} = \varepsilon_l - v\varepsilon_w$$

→ *Aside:* $\dfrac{dA}{A} = \dfrac{(H+dH)(W+dW)-HW}{HW} = \dfrac{(H-v(\varepsilon_l+\varepsilon_w)H)(W+(-v\varepsilon_l+\varepsilon_w)W)-HW}{HW}$

→ *Aside:* $\dfrac{dA}{A} = 1 - 2v\varepsilon_l + \varepsilon_w - v\varepsilon_w + (higher\ order\ terms) - 1$

→ *Aside:* $\dfrac{dA}{A} \approx -2v\varepsilon_l + \varepsilon_w - v\varepsilon_w$ *(for small strains)*

→ $\dfrac{\Delta R}{R} = \dfrac{dl}{l} - \dfrac{dA}{A} + \dfrac{d\rho}{\rho} \approx \varepsilon_l - v\varepsilon_w - (-2v\varepsilon_l + \varepsilon_w - v\varepsilon_w) + \dfrac{d\rho}{\rho}$

→ $\dfrac{\Delta R}{R} \approx (1 + 2v)\varepsilon_l - \varepsilon_w + \dfrac{d\rho}{\rho}$

→ $\Delta R_{total} \approx R\left[(1 + 2v)\varepsilon_a - \varepsilon_t + \left(\dfrac{d\rho}{\rho}\right)_a + \left(\dfrac{d\rho}{\rho}\right)_t\right]$

→ where the strain from part to grid, ε_l and ε_w, have been substituted for ε_a and ε_t, respectively and $\dfrac{d\rho}{\rho}$ has been broken into axial and transverse components

→ $\Delta R_{total} \equiv \Delta R_{geometric} + \Delta R_{change\ in\ resistivity}$
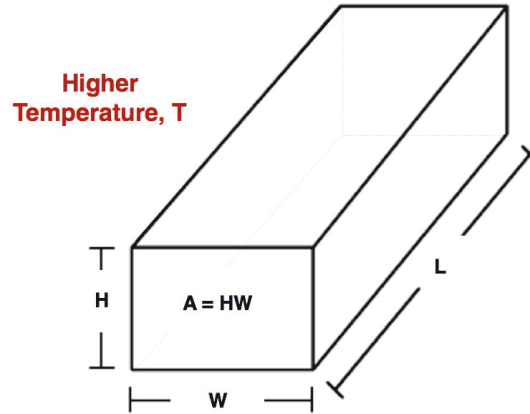
Higher Temperature, T

H

A = HW

W

L

Figure A. 3: Single Grid Approximation with Strain from Increased Temperature

$R = \rho\frac{l}{A},$ Linear expansion coefficient of the grid is α

→ $\Delta R = \frac{\partial R}{\partial l}dl + \frac{\partial R}{\partial A}dA + \frac{\partial R}{\partial \rho}d\rho = \frac{\rho}{A}dl - \frac{\rho}{A^2}dA + \frac{l}{A}d\rho$

→ $\frac{\Delta R}{R} = \frac{dl}{l} - \frac{dA}{A} + \frac{d\rho}{\rho}$

→ $Aside: \frac{dl}{l} = \frac{l\alpha\Delta T}{l} = \alpha\Delta T$

→ $Aside: \frac{dA}{A} = \frac{(H+dH)(W+dW)-HW}{HW} = \frac{(H+H\alpha\Delta T)(W+W\alpha\Delta T)-HW}{HW}$

→ $Aside: \frac{dA}{A} = \frac{HW+2HW\alpha\Delta T+HW(\alpha\Delta T)^2-HW}{HW} = 2\alpha\Delta T + [(\alpha\Delta T)^2 \approx 0]$

→ $\frac{\Delta R}{R} = \frac{dl}{l} - \frac{dA}{A} + \frac{d\rho}{\rho} \approx \alpha\Delta T - 2\alpha\Delta T + \frac{d\rho}{\rho}$

→ $\frac{\Delta R}{R} \approx -\alpha\Delta T + \frac{d\rho}{\rho}$

94

→ $\Delta R_{total} \approx R \left[-\alpha \Delta T + \dfrac{d\rho}{\rho} \right]$

→ $\Delta R_{total} \equiv \Delta R_{geometric} + \Delta R_{change\ in\ resistivity}$

→ In this case, the geometric change in resistance is driven by the thermal expansion of the part and is negative, while the change in resistivity is driven by the TCR of the strain gauge material

Appendix B

Model Dimensions

Model: EA-06-062AP-120/E
- EA: Constantan foil
- 06: Type of temperature compensation
- 062AP: (Dimensions)
- 120: Resistance =120ohms
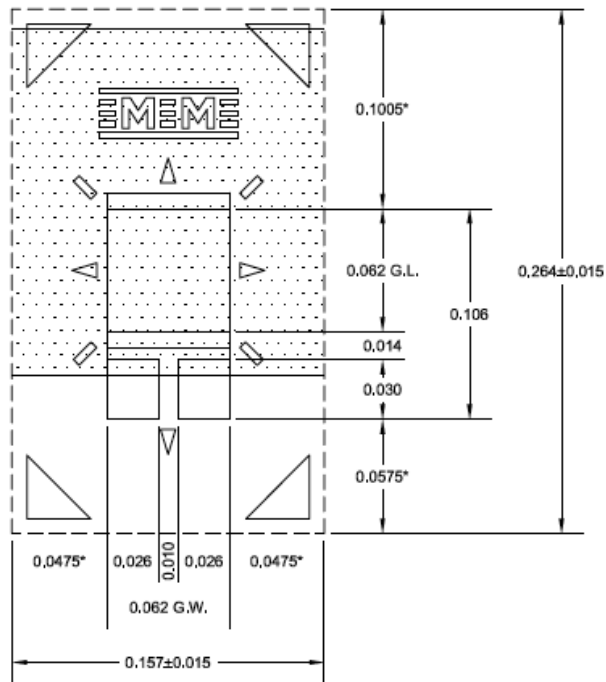- E: Gauge encapsulated in polyimide with exposed solder tabs

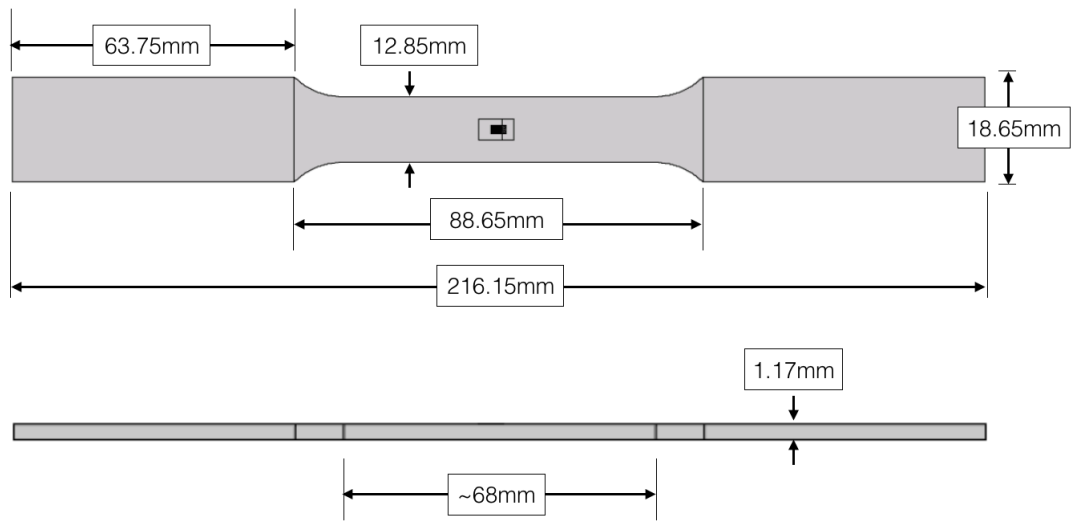*Figure B. 1: Strain Gauge Dimensions [44] for Model EA-06-062AP-120/E*

Figure B. 2: Dimensions of Tensile Coupon

Appendix C

Conventional Strain Gauge Thermal Test

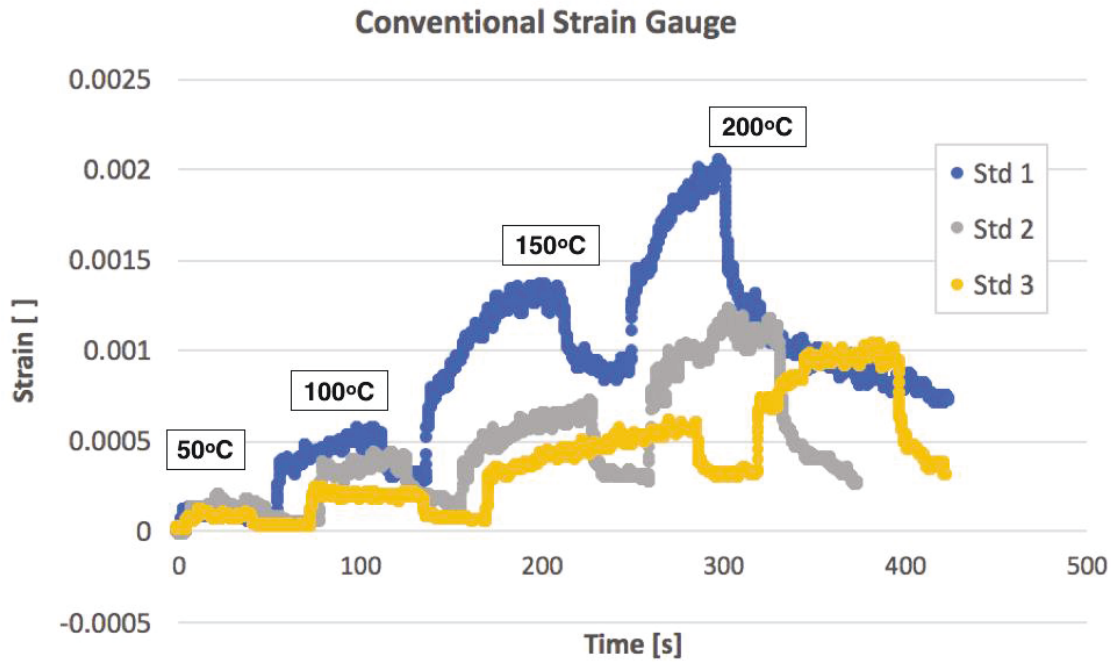Each strain gauge was subjected to an environmental temperature of 50, 100, 150 and 200ºC

Figure C. 1: Thermal Testing of Three Conventional Strain Gauges